Ocean Engineering 321 (2025) 120345

Contents lists available at ScienceDirect

Ocean Engineering

journal homepage: www.elsevier.com/locate/oceaneng

Research paper

Energy rate balance applied to coastal engineering problems by using RANS-VoF models in numerical wave flumes

Teixeira P R F[a,*], Didier E[b]

[a] Universidade Federal do Rio Grande, Rio Grande, Brazil
[b] Laboratório Nacional de Engenharia Civil, Lisbon, Portugal

ARTICLE INFO

Keywords:
RANS models
Numerical wave flume
Coastal engineering
Energy rate balance
Oscillating water column wave energy converter
Rubble-mound breakwater

ABSTRACT

Nowadays, the use of RANS-based models for simulating numerical wave flumes and studying coastal engineering structures is common and allows investigating accurately phenomena that occur in current/wave-structure interactions. Comprehension of energy transformations in these processes can support designers to optimize the system. In this study, a methodology to evaluate the terms of the energy rate balance in coastal engineering problems is developed. The methodology is applied to the propagation of regular waves in numerical wave flumes, onshore oscillating water column wave energy converter integrated into a vertical breakwater, and two types of rubble-mound breakwaters. The direct determination of the energy rate due to viscous and turbulence losses and the porous resistance in rubble-mound breakwaters are carried out by time integration inside the computational domain. Besides, the reflected and transmitted energy rates in the flume are calculated by means of this methodology, instead of the standard gauge methods, commonly used in physical and numerical flumes. Complementary, studies may be carried out for random incident waves and the methodology can be applied to 3D wave tanks.

1. Introduction

Several cases have been studied by coastal engineers to understand the current/wave-structure interactions, such as breakwaters and wave renewable devices. Physical experiments have an important contribution in this context; however, this type of investigation is dependent on the instrument limitations and uncertainties. Numerical approaches also have their restrictions, mainly related to the limited computational capacity to use accurate models based on Navier-Stokes equations in coastal engineering problems. Nevertheless, a great advantage of numerical models is the possibility to set and control any variable of the phenomenon to better understand the behavior of the system. Besides, the numerical modeling allows monitoring any variable that is very difficult to be measure in physical modeling throughout the whole study domain.

A complete and consistent study about the energy rate balance in numerical wave flumes by using Navier-Stokes equations allows a deeper understanding of the involved phenomena and the accuracy of the adopted numerical approach. A gap of knowledge in the numerical simulation of wave flumes is, for example, the quantification of the influence of the growing of the numerical dissipation along time caused by turbulence models and the energy loss of the incident wave, observed by several authors, such as Larsen and Fuhrman (2018) and Didier and Teixeira (2022).

Another interesting study topic is the quantification of the efficiency of any coastal structure to have conditions to optimize its design and operation. For example, the design of a wave energy converter can be improved if engineers understand how the energy is spatially distributed in the system along the time and, therefore, losses can be diminished to improve the extracted energy. There are many researches that use the high-fidelity numerical modeling to analyze the performance of several types of the wave energy converters, as those cited by Penalba et al. (2017), Windt et al. (2018), and Opoku et al. (2023). However, there are few works that investigated the energy balance around wave energy converters, such as Elhanafi et al. (2016), Tseng et al. (2000), Güths et al. (2022) and Teixeira and Didier (2023). In these studies, the incident wave energy is composed of the reflected wave energy, device extracted energy and dissipation of energy due to the viscous and turbulence losses. However, the latter is not directly evaluated, since it is the rest of energy that satisfies the energy balance. Therefore, some

* Corresponding author.
E-mail addresses: pauloteixeira@furg.br (T. P R F), edidier@lnec.pt (D. E).

https://doi.org/10.1016/j.oceaneng.2025.120345
Received 10 May 2024; Received in revised form 18 December 2024; Accepted 7 January 2025
Available online 17 January 2025

questions must be answered, such as: (i) How the mean viscous and turbulence losses can be directly determined? (ii) Are these values actually close the energy rate balance equation? (iii) How these losses are spatially distributed along the numerical flume?

Additionally, it is very important to understand how energy losses and damping of energy are distributed in a coastal engineering structure, such as a rubble-mound breakwater, allowing the improvement of their design and efficiency. There are many highlighted works about hydrodynamics of breakwaters such as Hsu et al. (2002), del Jesus et al. (2012), Higuera et al. (2014), Vanneste and Troch (2015), among others; however, the real spatial distribution of the energy losses out and inside the breakwater has not been studied yet. This information is very important to quantify the mean energy losses due to viscous and turbulence effects and the presence of porous media of the breakwater.

This study aims determining different types of energy rates in the energy rate balance equation of numerical wave flumes used in coastal engineering problems. Numerical simulations are carried out by using the ANSYS-FLUENT® (Ansys, 2016) numerical model, which is based on the Reynolds Averaged Navier-Stokes (RANS) equations and the Volume of Fluid (VoF) technique. The applicability of the developed methodology is shown in the wave propagation of regular waves in a numerical wave flume with horizontal bottom; numerical flumes with an onshore oscillating water column wave energy converter; and two types of rubble-mound breakwaters. It can be noted that the present methodology is not restricted to these examples; it can be applied to any coastal problem to understand how the energy rate is distributed in the system space.

2. The energy rate balance equation

The macroscopic balance of energy rate for isothermal flow in transient state results in the following equation (Bird et al., 2002):

$$\frac{dE_{tot}}{dt} = (\dot{E}_A - \dot{E}_B) + W_m + \dot{E}_c - \dot{E}_L \tag{1}$$

where E_{tot} is the total energy of the system, $\dot{E}_A$ and $\dot{E}_B$ are the internal, kinetic and potential energy rates and the liquid work that enters into the system through surfaces S_A (entrance) and S_B (exit), respectively; W_m is the work done by the surroundings on the fluid by means of moving surfaces; $\dot{E}_c$ is the mechanical energy rate due to the expansion and compression of the fluid, which is null when the fluid is assumed to be incompressible; and $\dot{E}_L$ is the dissipation rate of the mechanical energy due viscous forces.

The total energy of the system is composed of the sum of K_{tot} (kinetic energy) and Φ_{tot} (potential energy), i.e.:

$$E_{tot} = K_{tot} + \Phi_{tot} \tag{2}$$

which each term is given by:

$$K_{tot} = \int_{V(t)} \frac{\rho v^2}{2} dV \tag{3}$$

$$\Phi_{tot} = \int_{V(t)} \rho g y dV \tag{4}$$

where ρ is the specific mass, v is the magnitude of the fluid velocity, g is the gravitational acceleration, y is the vertical coordinate and $V(t)$ is the volume of the domain at the instant t. The energy rates that pass through surfaces S_A and S_B can be written as:

$$\dot{E}_A = \int_{S_A} \left(\frac{\rho_A v_A^3}{2} + \rho_A g y v_A + p_A v_A \right) dS_A \tag{5}$$

$$\dot{E}_B = \int_{S_B} \left(\frac{\rho_B v_B^3}{2} + \rho_B g y v_B + p_B v_B \right) dS_B \tag{6}$$

where p_A and p_B are the thermodynamic pressure on the surfaces A and B, respectively.

Differently from Bird et al. (2002), in which the term $\dot{E}_L$ is only due to the fluid viscous effect, in this study, it is composed by: $\dot{E}_{L\mu}$, which is the energy rate loss due to viscous and turbulent effects, and $\dot{E}_{Lp}$, which is the energy rate loss due to the flow into the porous media.

$\dot{E}_{L\mu}$ is always positive for Newtonian fluids and it is given by

$$\dot{E}_{L\mu} = \sum_i \sum_j \int_{V(t)} \left\{ \frac{\mu_e}{2} \left[\left(\frac{\partial v_i}{\partial x_j} + \frac{\partial v_j}{\partial x_i} \right) - \frac{2}{3} \frac{\partial v_k}{\partial x_k} \delta_{ij} \right]^2 \right\} dV \tag{7}$$

where i, j, $k = 1,2,3$, μ_e is the effective dynamic viscosity and δ_{ij} is the Kronecker delta. Equation (7) is adapted to turbulent flows, in which a Reynolds Averaged Navier-Stokes (RANS) based model is used, since μ_e is the sum of the fluid viscosity (μ) and the turbulent viscosity (μ_t), obtained by using a turbulent model.

The evaluation of $\dot{E}_{Lp}$ is carried out considering the methodology in which the volume averaging method (Whitaker, 1999) is employed in Navier-Stokes based models. This technique allows avoiding difficulties imposed by the complex geometry and small scales of the porous medium. It consists of using volumes whose the scale is larger than scales of porous structures that compose the porous media (Didier and Teixeira, 2022; Teixeira and Didier, 2023). Additionally, the momentum equations are extended by Darcy (linear) and Forchheimer (quadratic nonlinear) terms to consider the drag caused by the porous structure (van Gent, 1995; Didier and Teixeira, 2022). Therefore, the energy rate dissipation due to the porous media ($\dot{E}_{Lp}$) is given by (Nield, 2002; Vafai, 2005):

$$\dot{E}_{Lp} = \int_{V(t)} \left(\frac{\mu}{\alpha} v_i v_i + \frac{C_2}{2} \varrho |v| v_i v_i \right) dV \tag{8}$$

where $i = 1,2,3$, α and C_2 are permeability and inertial coefficients of the porous medium, respectively.

In this study, the energy rate balance is applied to numerical wave flumes, whose typical sketch is shown in Fig. 1. Navier-Stokes based models by using the Volume of Fluid (VoF) (Hirt and Nichols, 1981) method are considered to treat the two-phase oscillating flows. The moving surfaces are not involved in the energy rate balance equation Eq. (1), i.e., $W_m = 0$. Basically, there are losses inside the flume due to viscous and turbulence effects ($\dot{E}_{L\mu}$) and the porous resistance ($\dot{E}_{Lp}$) in cases of the presence of porous structures. Generally, the domain is composed by the following boundaries:

a) Wave maker: The velocity profiles and volume fraction are imposed every instant according to the incident wave characteristics. Therefore, this boundary is considered as the entrance of the energy source, in which the energy rate $\dot{E}_A$ passes through the surface S_A;
b) Bottom: It is considered impermeable and, consequently, the kinematic condition of non-slip condition is imposed. In isothermal flows, this boundary does not change energy with the soil;
c) Atmosphere: The atmospheric pressure is imposed. It could be considered as exit boundary; however, taking into account that the air specific mass is much lower than water one and it is imposed the atmospheric pressure, energy rate that passes through this boundary can be neglected;
d) Flume end: The radiation wave condition is imposed. Therefore, this boundary is considered as exit of the energy source, in which the energy rate $\dot{E}_B$ passes through the surface S_B.

After initial transient regime, the flow reaches the stable periodic regime and the mean time of terms of the energy rate balance equation, Eq. (1), is applied to numerical flumes taking into account regular incident waves. In this case, the mean time of the energy rate balance in the time integration form is given by:

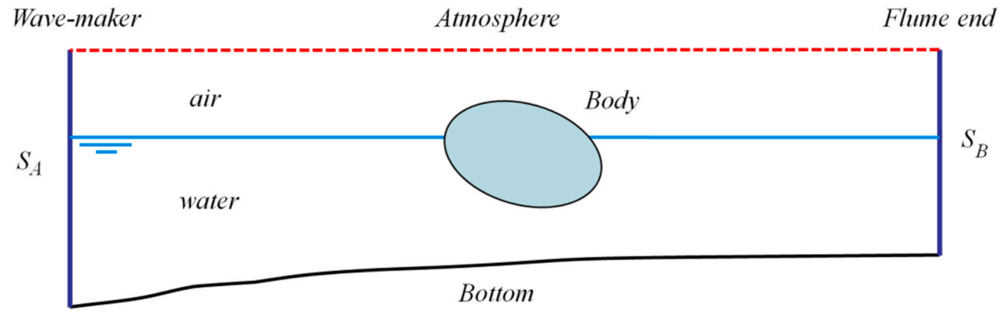

Fig. 1. Sketch of a typical numerical wave flume and definition of variables for energy rate balance.

$$(E_A - E_B) - E_L - \Delta E_{tot} = Res \tag{9}$$

where

$$\Delta E_{tot} = (E_{tot}(t_2) - E_{tot}(t_1)) \,/\, (t_2 - t_1) \tag{10}$$

$$E_A = \frac{1}{(t_2 - t_1)} \int_{t_1}^{t_2} \dot{E}_A \, dt \tag{11}$$

$$E_B = \frac{1}{(t_2 - t_1)} \int_{t_1}^{t_2} \dot{E}_B dt \tag{12}$$

$$E_L = E_{L\mu} + E_{Lp} = \frac{1}{(t_2 - t_1)} \int_{t_1}^{t_2} (\dot{E}_{L\mu} + \dot{E}_{Lp}) dt \tag{13}$$

where ΔE_{tot} is the time variation of the total energy of the system, E_A, E_B, and E_L are the mean energy rates along the time record duration $T_r = t_2 - t_1$. T_r is equal to the wave period T when the fluid flow achieves a stable periodic regime. *Res* is theoretically equal to zero but takes a small non-zero value due to inherent uncertainties of the numerical modeling.

In this study, E_{A0} is considered the mean energy rate imposed by the wave maker at the beginning of the simulation, before the reflected waves reach the wave maker; and E_A is the mean energy rate on the wave maker considering the presence of the reflected wave after the flow stabilization. Therefore, the mean reflected energy rate due to the reflected wave (E_R) may be calculated by the difference between mean energy rates E_{A0} and E_A on the wave maker and, consequently, the mean energy rate balance equation (Eq. (9)) can be rewrote as follows.

$$E_{A0} - \Delta E_{tot} - Res = E_R + E_{L\mu} + E_{Lp} + E_B \tag{14}$$

At the stable periodic regime, it is expected that *Res* and ΔE_{tot} are practically null; it means that the mean energy rate imposed by the wave-maker (terms of LHS of Eq. (14)) is approximately composed by the mean reflected energy rate (E_R), the mean energy rate due to viscous and turbulence losses ($E_{L\mu}$), the mean energy rate due to porous medium losses (E_{Lp}) and the mean energy rate E_B (terms of RHS of Eq. (14)).

3. Mathematical and numerical models

The general description of the mathematical and numerical models used in the study cases (wave propagation in a wave flume, OWC device, rubble-mound breakwaters) is shown in this Section. Specific characteristics of each case are complemented in Sections 4, 5, and 6, and detailed information can be obtained from the cited references of the authors that previously studied these cases.

3.1. Governing equations

In this study, the 2D free surface flow Navier-stokes equations are used, which are given by (Versteeg and Malalasekera, 2007):

$$\frac{\partial v_i}{\partial x_i} = 0 \tag{15}$$

$$\frac{\partial(\rho v_i)}{\partial t} + \frac{\partial(\rho v_i v_j)}{\partial x_j} = -\frac{\partial p}{\partial x_i} + \rho g_i + \frac{\partial \tau_{ij}}{\partial x_j} + S_i \tag{16}$$

$$\tau_{ij} = \mu\left(\frac{\partial v_i}{\partial x_j} + \frac{\partial v_j}{\partial x_i}\right) - \frac{2}{3}\mu \frac{\partial v_k}{\partial x_k}\delta_{ij} \tag{17}$$

$$\frac{\partial f}{\partial t} + u_j \frac{\partial f}{\partial x_j} = 0 \tag{18}$$

where i, $j = 1, 2$, ρ the specific mass, g_i the components of the gravitational acceleration, v_i the components of the velocity, p the pressure, S_i a source term. The source term depends on the case study and it can be related to the porous zone that represents the turbine effect inside the OWC chamber; and the porous media of rubble-mound breakwaters. τ_{ij} is the viscous stress tensor and μ is the viscosity. The VoF transport equation, Eq. (18), allows tracking the free surface.

The RANS equations are used and different turbulence models are adopted in this study, depending on the problems to be simulated.

3.2. Numerical model characterization

The ANSYS-FLUENT® software (Ansys, 2016) is used for numerical simulations of the 2D wave flume. In all study cases, the algorithm SIMPLEC is used for the pressure-velocity coupling. The PRESTO! method is used for spatial discretization of pressure, whereas the interpolation scheme of third-order MUSCL is adopted for momentum and turbulence. These methodologies have employed by Teixeira et al. (2017), Didier et al. (2017), Mendonça et al. (2018), Lisboa et al. (2018), Teixeira et al. (2020), Wiener et al. (2022) and Teixeira and Didier (2023).

Two numerical models are used depending on the type of free surface flow: the implicit and explicit numerical models. The implicit model is perfectly adapted to wave propagation and wave-structure interaction without wave breaking, whereas the explicit model is used for large deformation of the free surface, as occurs for wave breaking and wave overtopping of structures. The characteristics of each model are:

- The implicit model uses a second order implicit scheme for time integration, six non-linear iterations per time step, and time step below $T/600$. The HRIC method (Péric and Ferziger, 1997) is employed for tracking the free surface (Lisboa et al., 2018; Teixeira et al., 2020; Wiener et al., 2022). The model is adopted for wave propagation (Section 4) and wave interaction with the OWC device (Section 5). Under-relaxation coefficients used for the SIMPLEC algorithm are equal to 1 for the momentum, pressure, density, and VoF;
- The explicit model uses a first order time integration scheme, and a variable time step with a Courant number of 0.7. The Geo-reconstruct scheme is used for the tracking the free surface (Didier and Teixeira, 2022, 2023). In this work, the model is employed to cases with rubble-mound breakwaters (Section 6). Relaxation

parameters used in the SIMPLEC algorithm are 0.7 for the momentum, 0.3 for the pressure, and 1.0 for the density.

The turbulence model is chosen for each study case according to the complexity of the wave-structure interaction and the objective of minimizing the numerical dissipation induced by some turbulence models (Larsen and Fuhrman, 2018; Didier and Teixeira, 2022, 2023). The case of wave propagation (Section 3) quasi does not involve turbulence dissipation which means that the flow is nearly potential. It is neither recommended nor necessary to use a turbulence model, which can generate numerical dissipation. Therefore the free surface flow is considered laminar and the RANS equations, Eqs. (15)–(17) degenerate into Navier-Stokes equations. In the other cases of wave-structure interactions, a turbulence model is required. The case of the OWC device (Section 4) is relatively straightforward since incident waves interact smoothly with the impermeable structure, and the k-ω SST hybrid turbulent/laminar model is used (Didier and Teixeira, 2023). The laminar zone is applied to the wave propagation region of the wave flume, from the wave maker to 10 m from the front wall of the OWC device. The case of rubble-mound breakwaters involving complex free surface interactions with the porous structure requires using the $k-\varepsilon$ NLS turbulence model (Shih and Zhu, 1996), which shows higher agreement results with experimental ones (Didier and Teixeira, 2022, 2023). Small values of turbulence kinetic energy ($k = 10^{-6}\ \mathrm{m^2/s^2}$) and dissipation rate ($\varepsilon = 10^{-6}\ \mathrm{m^2/s^2}$) or specific dissipation rate ($\omega = 1\ \mathrm{s^{-1}}$) are imposed following Lin and Liu (1998) and Elhanafi et al. (2016).

Although each case has its own boundary conditions, some of them are general and applied to all cases. The non-slip condition is imposed on the wave flume bottom. The atmospheric pressure is applied to the top boundary of the wave flume. The numerical wave maker for the wave generation is used at the boundary S_A, in which velocity components and volume fraction are imposed at each instant. The active absorption technique is applied to the boundary S_A and the end of the wave flume (S_B), when necessary, to eliminate the effects of the re-reflected waves inside the wave flume. This method was validated and applied by Didier et al. (2017), Mendonça et al. (2018), Teixeira et al. (2020) and Teixeira and Didier (2023) for 2D wave flumes, Lisboa et al. (2017) and Teixeira and Didier (2021) for random waves in 2D flumes, and Teixeira et al. (2017) and Didier and Teixeira (2024) for 3D wave tanks by means of User Defined Functions (UDF).

The initial conditions adopted for all cases are: the free surface level at rest, null velocity components, hydrostatic pressure on the water, and atmospheric pressure on the air.

The computational mesh of the wave flume with a structure has at least two main zones with different mesh characteristics: the propagation wave zone and the zone around the structure. In the former, a structured regular mesh is used, in which the free surface is well behaved, and the mesh must be refined around it. Mesh resolution for accurate wave propagation is defined by 70 cells per wavelength in the horizontal direction, with a refinement near the wave maker and wall boundaries, and 20 cells per wave height in the vertical direction, in the zone of variation of free surface flow defined with a height of $2H$, and a mesh stretching to the bottom and top of the flume (Mendonça et al., 2018; Teixeira and Didier, 2021; Didier and Teixeira, 2022, 2023). In the zone around the coastal structure, the flow can have a complex behavior, including wave breaking and overtopping; therefore, regular cells are recommended to have an aspect ratio close to 1 (Brown et al., 2016; Devolver et al., 2018). In the OWC device, a structured regular mesh around the OWC walls are used, according to Mendonça et al. (2018), Teixeira et al. (2020) and Güths et al. (2022). In the case of the breakwaters an unstructured mesh using regular cells around and inside the coastal structure is employed (Didier and Teixeira, 2022).

3.3. Monitoring

The variables that compose the balance of the energy rate are defined in the “custom field function calculator” tool of the ANSYS-FLUENT® software. The energy rates, $\dot{E}_A$ and $\dot{E}_B$, are integrated on S_A and S_B boundaries, and the terms $\dot{E}_L$ and E_{tot} are integrated in the domain zones during the execution process. The terms of the balance of the energy rate, Eq. (9), are calculated in the post-process.

In all study cases, the reflect wave coefficient (C_R) is determined by using the three-gauge method (Mansard and Funke, 1980). This method allows calculating the reflected wave coefficient (C_R) by means of three gauges on the flume, in which the second and third gauges are $0.1L$ and $0.27L$ from the first gauge, respectively. Some authors, such as Güths et al. (2022) and Teixeira and Didier (2023), calculate the relation between the mean reflected energy rate and the mean energy rate imposed by the wave maker by using the C_R calculated by the three-gauge method. Therefore, the relation between the mean reflected energy rate and the one imposed by the wave maker can be considered equal to C_R^2.

4. Progressive and standing waves in a numerical wave flume

4.1. Study case and mathematical model

The methodology to determine the energy rate balance is firstly applied to the progressive and standing waves, based on the second-order Stokes wave theory (Dean and Dalrymple, 2000), in a 2D numerical wave flume 10 m deep and $4L$ long (where L is the wavelength) (Fig. 2). The incident regular waves with periods from 6 to 12 s every 1 s and $H = 1.5$ m are imposed by means of a wave maker. In the case of the standing waves, a slip condition is imposed on the vertical wall to the end of the wave flume (S_B), which means that E_B is null.

In these cases, E_A and E_B of the energy rate balance equation are the mean energy rates at the beginning (boundary S_A) and the end (boundary S_B) of the wave flume, respectively. The energy rate on the top boundary is considered null, since it is imposed the atmospheric pressure and the momentum of the air is insignificant in comparison to the involved momentum of the water. The unique energy dissipation is due to the viscous stress of the water flow ($E_{L\mu}$), which is considered laminar.

In this study, E_{A0} is the mean energy rate imposed by the wave maker at the beginning of the simulation (from instants $t = 3T$–$4T$), E_A is the mean energy rate on the wave maker obtained by considering the presence of the reflected wave detected by the active absorption technique after the flow stabilization, and E_R is the mean reflected energy rate due to the reflected wave, which is obtained by the difference between E_{A0} and E_A.

4.2. Progressive wave with $T = 8$ s

In this Section, the time series of the free surface elevation inside the flume (η), the energy rates on the wave maker ($\dot{E}_A$) and the end boundary ($\dot{E}_B$) and total energy inside the flume (E_{tot}) are discussed for the incident wave with $T = 8$ s, which is an intermediate period in the range 6–12 s.

Fig. 3a shows the time series of the free surface elevation located at $2L$ from the wave maker. It can be observed that the free surface elevation stabilizes in a periodic behavior after around 15 wave periods. The wave height after stabilization is $H = 1.501$ m, which is almost the same value as the incident wave height imposed on the wave maker. This fact shows the efficiency of the active absorption technique applied to the wave generation and the end of the flume, which allows simulating a semi-infinite wave flume.

Fig. 3b and c shows the time series of the energy rates on the wave maker ($\dot{E}_A$) and the end boundary ($\dot{E}_B$) of the flume and the time series of the total energy inside the flume (E_{tot}), respectively. It can be noticed in Fig. 3b that the energy rate on the end boundary ($\dot{E}_B$) is initially null and, after a short duration of a transient regime, it maintains a behavior very

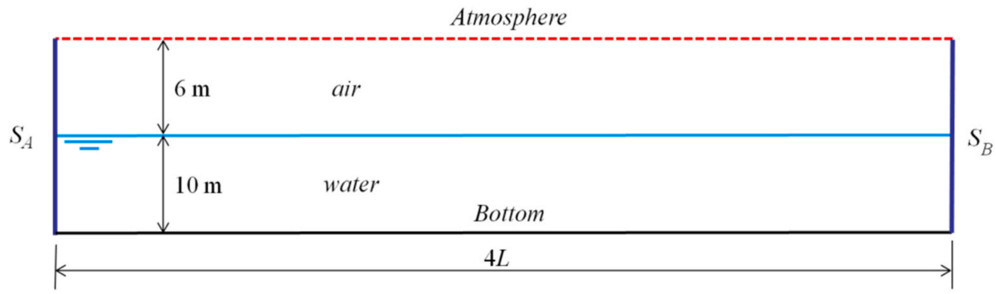

Fig. 2. Computational domain of progressive and standing waves in the numerical flume.

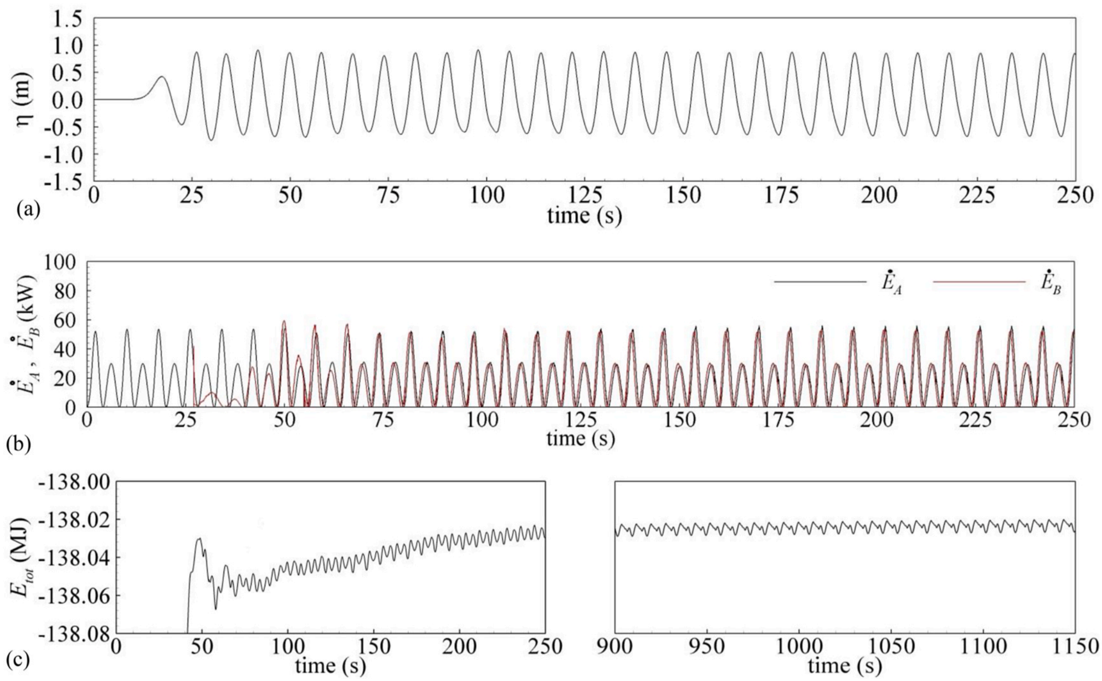

Fig. 3. Progressive wave with $T = 8$ s: Time series of (a) the free surface elevation located at $2L$ from the wave maker, (b) the energy rates on the wave maker (black line) and the end boundary (red line) of the flume, and (c) the total energy inside the flume. (For interpretation of the references to colour in this figure legend, the reader is referred to the Web version of this article.)

similar to the one of the energy rate imposed in the wave maker ($\dot{E}_A$). The total energy inside the flume (E_{tot}), Fig. 3c, shows a transient duration at the initial time of the wave generation and reaches a practical stability after around 900 s. This fact allows concluding that in this case, even if the wave height in the flume stabilizes after around 15 wave periods, the total energy inside the wave flume needs more than 100 wave periods to reach stabilization.

4.3. Standing wave with $T = 8$ s

In this Section, the time series of the free surface elevation (η), the energy rates and total energy inside the flume are discussed for the incident wave with $T = 8$ s. Fig. 4a shows the time series of the free surface elevation located at $2L$ from the wave maker. Stabilization is reached after around 15 wave periods, which is enough time to stabilize the propagation along the flume of the reflected wave caused by the vertical wall at its end. The wave height after stabilization is $H = 2.959$ m, which is very similar to the expected theoretical value for a fully reflected wave in a flume with a vertical wall at its end (3.0 m).

Fig. 4b and c shows the time series of the energy rates on the wave maker of the flume ($\dot{E}_A$) and the total energy inside the flume (E_{tot}), respectively. Initially, $\dot{E}_A$ is imposed by the wave maker without the effect of the active absorption technique and, thereafter, the active absorption is applied to avoid the re-reflected wave inside the flume and, consequently, the reflected energy rate. It may be noticed that the active absorption is activated at instant 64 s, which is before the first reflected wave from the wall at the end of the wave flume reaches the wave maker. This explains the increase of the energy rate at the wave maker around this time (Fig. 4b), which reduces substantially in a few waves before stabilizing indicating that periodic free surface flow has been established. The total energy inside the flume (E_{tot}), Fig. 4c, shows a transient duration since the initial of the wave generation and reaches practical stability after around 300 s, which is higher than the stabilization time of the free surface elevation.

4.4. Analysis of energy rate balance for progressive and standing waves at periods from 6 to 12 s

In this Section, the mean energy rates of the numerical wave flume in progressive and standing waves are discussed for the incident wave with T from 6 to 12 s.

Table 1 shows the terms of the mean energy rate balance equation, Eq. (9), for progressive waves. Residues of the energy rate balance equation (Res) are lower than 1.3% of the mean energy rate E_{A0}. The time variation of the total energy of the flume (ΔE_{tot}) is very low for all

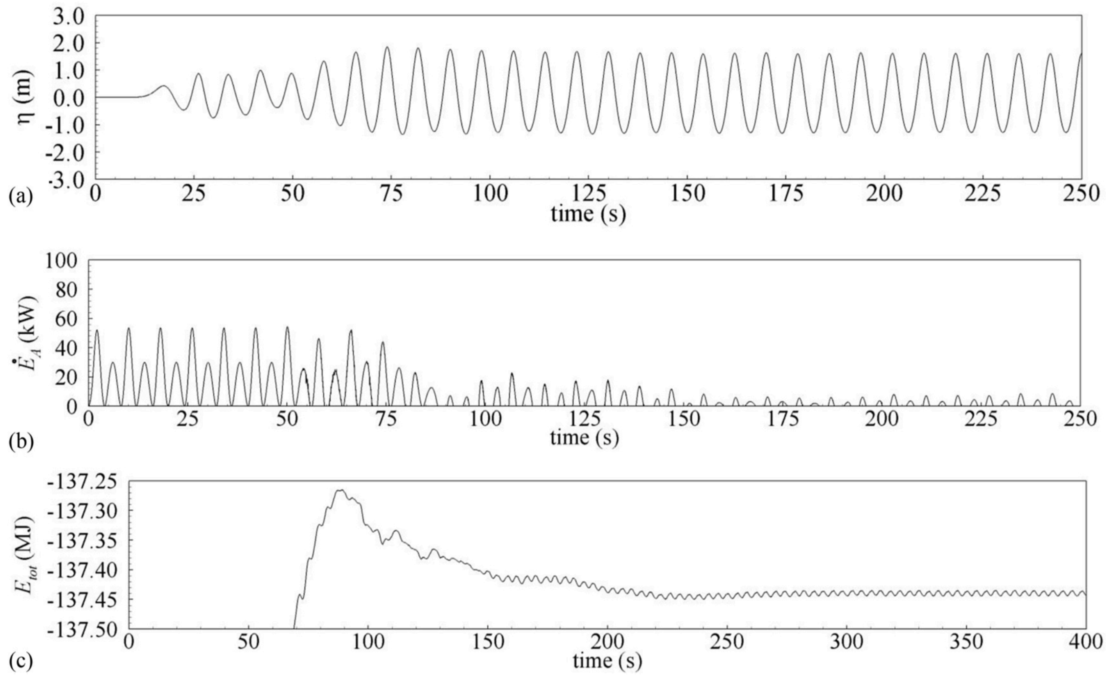

Fig. 4. Standing wave with $T = 8$ s: Time series of (a) the free surface elevation located at $2L$ from the wave maker, (b) the energy rates on the wave maker of the flume and (c) the total energy inside the flume.

Table 1
Mean energy rates of the numerical wave flume in progressive wave cases.

T (s)	E_{A0} (kW/m)	E_A (kW/m)	E_R (kW/m)	E_B (kW/m)	E_L (kW/m)	ΔE_{tot} (kW/m)	Res (kW/m)	Res/E_{A0} (%)
6	15.91	14.65	1.26	14.44	0.00	0.00	0.21	1.3
7	18.44	17.53	0.91	17.34	0.00	0.01	0.17	0.9
8	20.40	19.93	0.47	19.76	0.00	0.00	0.16	0.8
9	21.97	21.79	0.18	21.59	0.00	0.02	0.18	0.8
10	23.31	22.71	0.60	22.56	0.00	0.00	0.15	0.6
11	24.44	24.10	0.34	23.94	0.00	−0.02	0.18	0.7
12	25.49	21.17	0.32	25.02	0.00	0.00	0.16	0.6

incident wave periods, which is insignificant in relation to E_{A0}. It shows that the periodic regime is practically stable at the record duration used to measure the mean energy rates. The dissipation energy rate E_L is only due to the viscous effect ($E_{L\mu}$) and it is in order of magnitude of 10^{-3} kW/m, which characterizes a near-potential flow, as expected. The mean reflected energy rate E_R is low, whose highest value occurs at $T = 6$ s, which represents 8% of the incident wave energy. The mean energy rate E_B, at the end of the flume, is very similar to E_A, with differences due to the low mean reflected energy rate and numerical modeling uncertainties.

Table 2 shows the terms of the mean energy rate balance equation for standing waves. Residues of the energy rate balance equation are very low, which are lower than 1.4% from the mean energy rate imposed by the wave maker E_{A0}. The time variation of the total energy inside the flume (ΔE_{tot}) is also very low, which shows that the flow is periodically stable at the record duration used to calculate the terms of the energy rate balance equation. The dissipation energy rate ($E_{L\mu}$) is in the order of the magnitude of 10^{-3} kW/m, since the flow is laminar with a low level of dissipation in this case. In this case, E_B is null because at the boundary S_B there is a vertical wall. E_R is almost equal to E_{A0}, which represents the presence of a standing wave in the flume.

Table 2
Mean energy rates of the numerical wave flume in standing wave cases.

T (s)	E_{A0} (kW/m)	E_A (kW/m)	E_R (kW/m)	E_B (kW/m)	E_L (kW/m)	ΔE_{tot} (kW/m)	Res (kW/m)	Res/E_{A0} (%)
6	15.91	0.11	15.80	0.00	0.00	0.00	0.12	0.7
7	18.44	0.06	18.38	0.00	0.00	0.00	0.06	0.4
8	20.40	0.00	20.40	0.00	0.00	0.00	0.00	0.0
9	21.97	0.04	21.93	0.00	0.00	0.02	0.02	0.1
10	23.31	0.09	23.22	0.00	0.00	0.00	0.08	0.4
11	24.44	0.20	24.24	0.00	0.00	0.02	0.18	0.8
12	25.49	0.37	25.12	0.00	0.00	0.00	0.36	1.4

Table 3 shows the relation between the mean reflected wave energy rate and the mean energy rate imposed on the wave maker by using the energy rate balance methodology (E_R/E_{A0}) and the three-gauge method (C_R^2) for progressive and standing wave cases, considering the first gauge at $2L$ from the wave maker. In the case of the progressive waves, the theoretical value of reference is null. Values obtained by both methods are very low. However, the higher differences between them are observed at lower wave periods, probably because of the effect of the active absorption technique, which is based on the wave propagation in shallow water condition. Therefore, this hypothesis can cause more uncertainties for wave propagation with low wave periods.

In the case of the standing waves, the theoretical expected value is 1. Both methodologies presented values from 0.99 to 1.01 and, therefore, very good agreement is observed. It may be emphasized that, different

Table 3
Mean reflected wave energy rate in relation to the mean energy rate imposed on the wave maker by using the energy rate balance methodology (E_R/E_{A0}) and the three-gauge method (C_R^2) for progressive and standing wave cases.

T (s)	Progressive waves		Standing waves	
	E_R/E_{A0}	C_R^2	E_R/E_{A0}	C_R^2
6	0.08	0.02	0.99	1.01
7	0.05	0.01	1.00	1.00
8	0.02	0.01	1.00	1.00
9	0.01	0.00	1.00	1.00
10	0.03	0.01	1.00	1.00
11	0.01	0.01	0.99	1.00
12	0.01	0.01	0.99	0.99

from flumes used for progressive waves, the wave maker boundary is unique responsible for eliminating the reflected wave, once at the end of the flume there is a vertical wall. Therefore, uncertainties caused by the active absorption technique for waves with low periods are minimized.

5. Numerical wave flume with an onshore OWC-WEC

5.1. Study case and mathematical model

Investigation of incident regular waves with periods $T = 6, 7, 8, 9, 10, 11, 12$ s and height $H = 1.5$ m in a wave flume with an onshore OWC on its end is carried out. The 2D wave flume, Fig. 5, is 10 m deep and $4L$ long up to the front wall of the OWC device. The OWC chamber is 10 m long and 10 m wide, with the front wall 0.5 m thick and the submergence depth of 2.5 m. The device is equipped with a Wells turbine whose characteristic relation, k_t, is 100 Pa s m^{-3}. This layout has previously adopted by Teixeira and Didier (2021), Güths et al. (2022) and Teixeira and Didier (2023).

A porous zone located in two layers of cells adjacent to the top boundary S_B is considered, to take into account the effect of the Wells turbine damping, by using source terms S_i of the momentum equations, Eq. (16). S_i and the time mean pneumatic power (P_t) available to the Wells turbine are detailed in Güths et al. (2022).

5.2. Energy rate balance equation applied to the onshore OWC device

In this specific study, the system is composed of the wave flume and the OWC device. The mean energy rate balance equation, Eq. (9), applied to the system, results in following terms:

a) E_A is the mean energy rate measured at the wave maker boundary S_A, which is composed of the mean energy rate imposed to the wave maker boundary due to the incident wave (E_{A0}) deducted from the mean reflected wave energy rate (E_R), due to the presence of the OWC device at the end of the wave flume. This composition is directly considered in the numerical model by means of the use of the active absorption technique.
b) E_B is the mean energy rate that passes through the top boundary S_B of the OWC air chamber, in which the atmospheric pressure is imposed. The energy rate on the top boundary of the wave flume is considered neglected.
c) E_L is composed of:
   i The mean energy rate losses due to the fluid viscosity and turbulence effects ($E_{L\mu}$), which are composed of mean energy rate losses in the propagation region (laminar flow) ($E_{L\mu 1}$) and region around the front wall and inside the chamber of OWC ($E_{L\mu 2}$), and;
   ii The mean energy rate losses due to the porous zone that represents the damping of the turbine on the air OWC chamber (E_{Lp}), which is calculated by means of Eq. (13), considering $C_2 = 0$ in Eq. (8) ($\dot{E}_{Lp}$) for a Wells turbine. This is the same value of the time mean pneumatic power (P_t), obtained by means of Eq. (20).

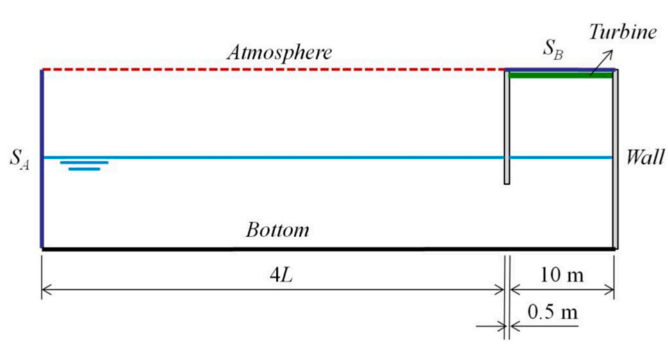

Fig. 5. Computational domain for the onshore OWC in numerical wave flume.

5.3. Detailed analysis for the incident wave with $T = 8$ s

Fig. 6 shows the time series of the mean free surface elevation inside the OWC chamber and the mean air pressure inside the air chamber for the incident wave with $T = 8$ s and $H = 1.5$m. After the transient regime until around 160 s ($20T$), the periodic stable behavior of the interaction between the incident wave and the OWC is reached.

Fig. 7 shows the time series of the energy rate imposed by the wave maker ($\dot{E}_A$), energy rate losses due to viscosity and turbulence effects ($\dot{E}_{L\mu}$), energy rate losses due to the porous medium that, in this case, represents the damping of the turbine ($\dot{E}_{Lp}$), and the total energy inside the system (E_{tot}). It can be observed that all variables show a stable periodic behavior at the end of the record. Besides, after around 60 s (approximately $8T$), there is some variation of $\dot{E}_A$, due to the presence of the reflected wave energy on the wave maker boundary. This phenomenon also affects the behavior of the other variables ($\dot{E}_{L\mu}$, $\dot{E}_{Lp}$ and E_{tot}). The stabilization of the total energy inside the system, Fig. 9d, occurs at the end of the record, which is about 600 s ($75T$).

Fig. 8 shows the contour of the velocity magnitude and streamlines, and the energy rate losses due to the viscous and turbulence effects ($\dot{E}_{L\mu}$). $t = 0$ is the instant when the zero up-crossing of the mean free surface inside the OWC chamber occurs and the flow enters inside the chamber; the velocity magnitude is higher around the submerged corner of the lip and it is lower around the corner between the back wall of the chamber and the bottom; it causes a high concentration of the energy rate losses around the submerged corner of the lip and, with less intensity, at the external part of the frontal wall of the chamber near the free surface. At $t = T/4$, the free surface elevation inside the chamber is practically the maximum one and, consequently, the velocity magnitude of the water inside the chamber is very low; however, it is observed a flow rotation around the internal part of the frontal wall, that contributes to increase the energy rate losses in this region. $t = T/2$ is the instant when the zero down-crossing of the mean free surface inside the chamber occurs and the water flows out of the chamber; in a region below the submerged corner of the lip, the velocity magnitude is higher, which causes the increase of the energy rate losses. At $t = 3T/4$, the free surface inside the chamber is practically the minimum one and, similarly to the instant $t = T/4$, velocity magnitude inside the chamber is very low; it is observed a concentration of moderate intensity of the energy rate losses outside the chamber below the corner of the lip, because of some flow rotation in this zone.

Fig. 9 shows the contour of the time average of the energy rate losses per volume due to the viscous and turbulence effects. It can be observed that the effect of the turbulence is very significant and concentrated around the lip of the front wall of the chamber. This is an expected result, since it is the zone where higher velocity gradients occur in the flow, due to the periodic water transfer between the outside and inside the device.

5.4. Analysis of energy rate balance for incident waves at periods from 6 to 12 s

In this Section, terms of the mean energy rate balance are determined for the flume with the onshore OWC device, considering incident regular waves with periods from 6 to 12 s and wave height of 1.5 m. The mean energy quantities that compound terms of the energy balance are shown in Table 4. Residues (Res) of all cases are lower than 3.4% of the mean energy rate imposed by the wave maker (E_{A0}). The highest values of Res occur at the lowest wave periods, probably due to the uncertainties caused by the hypothesis of the shallow water condition considered in the active absorption technique imposed on the wave maker boundary, as observed previously in Section 4 for progressive waves in wave flume. The time variation of the total energy inside the flume (ΔE_{tot}) is very low (practically null), which shows that the variables of the flow are stabilized in the recording interval and all quantities are well estimated. In all

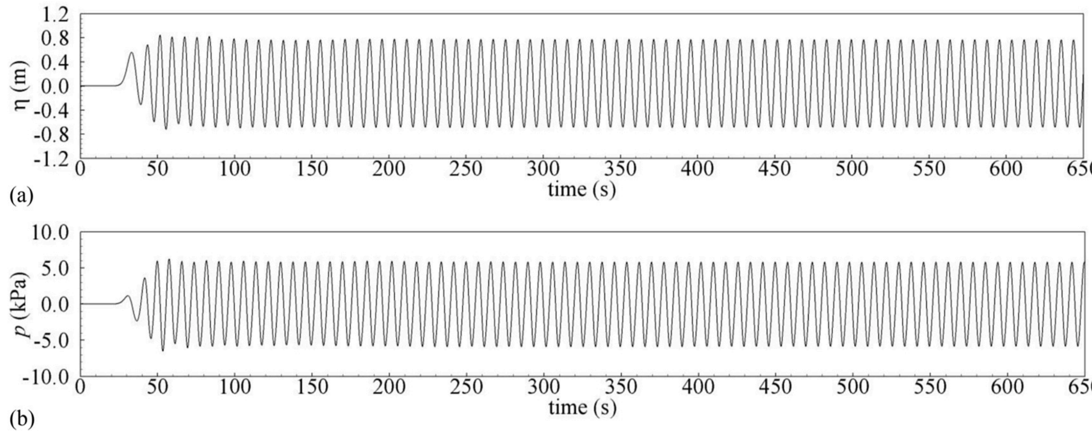

Fig. 6. Time series of (a) the mean free surface elevation inside the chamber and (b) the mean air pressure in the OWC air chamber.

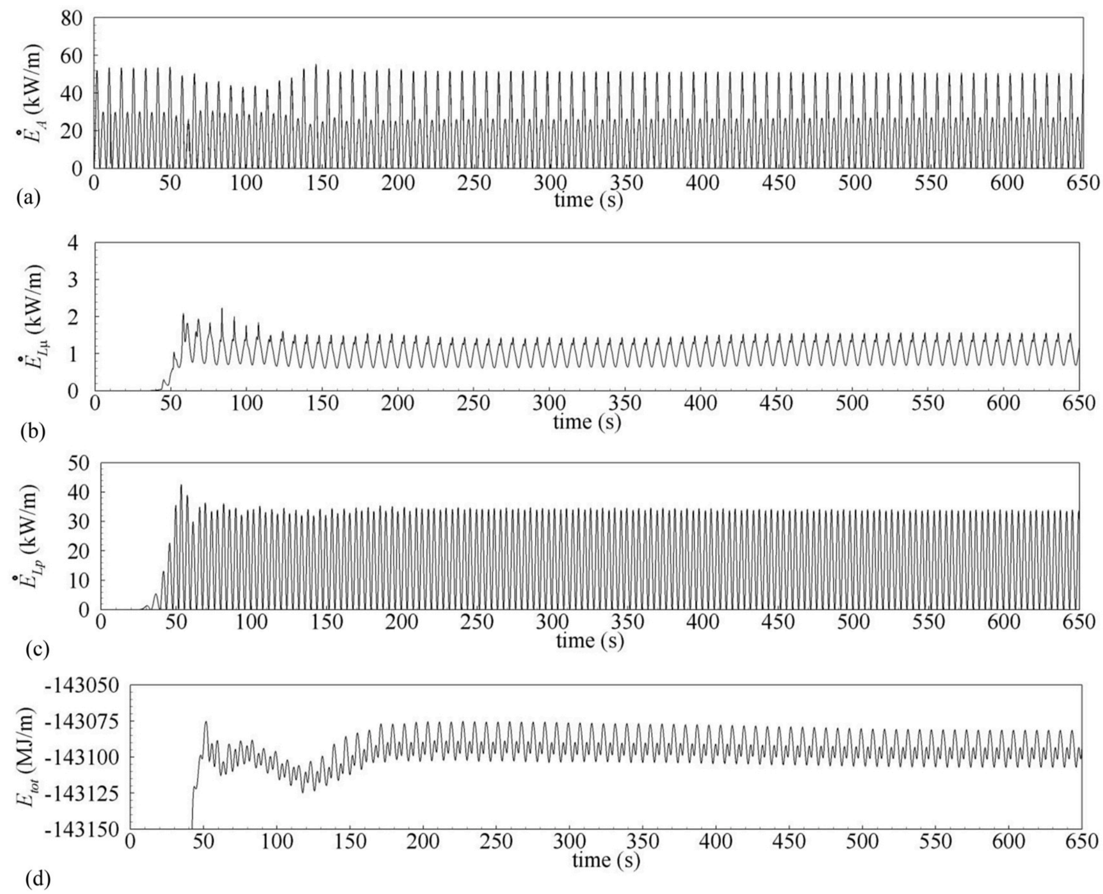

Fig. 7. Time series of (a) energy rate imposed by the wave maker ($\dot{E}_A$), (b) energy rate losses due to viscosity and turbulence effects ($\dot{E}_{L\mu}$), (c) energy rate losses due to the damping of the turbine ($\dot{E}_{Lp}$), and (d) the total energy inside the system (E_{tot}).

cases, E_B, which represents the mean energy rate that passes by the top of the air chamber, is practically null (in the order of magnitude of 10^{-4} kW/m), because at the boundary S_B is imposed the atmospheric pressure. The mean energy rate losses due to viscous and turbulence effects in the wave propagation region of the flume is practically null. It is because the hybrid turbulent *k*-*ω* SST/laminar model is used, which means that a laminar flow is applied to the wave propagation region of the flume. Therefore, $E_{L\mu}$, shown in Table 4, corresponds to the contribution of the zone around and inside the OWC device. It can be noted that $E_{L\mu}$ is around 1.00 kW/m and it does not vary significantly with the wave period. E_{LP}, which is calculated by considering the porous medium inside the air chamber, corresponds to the pneumatic power which passes by the Wells turbine and it is the highest term of the energy rate balance, as expected. The maximum value E_{LP} occurs around $T = 9$ s, which corresponds to the maximum pneumatic power defined by previous study of Güths et al. (2022) for similar conditions. E_R increases with the wave period, which indicates that wave reflection in the flume increases.

The mean reflected energy rate in relation to the mean energy rate imposed by the wave maker (E_R/E_{A0}) can be compared with the square reflected wave coefficient (C_R^2) obtained by the three-gauge method, using the first gauge at $2L$ from the wave maker. Fig. 10a shows E_R/E_{A0}

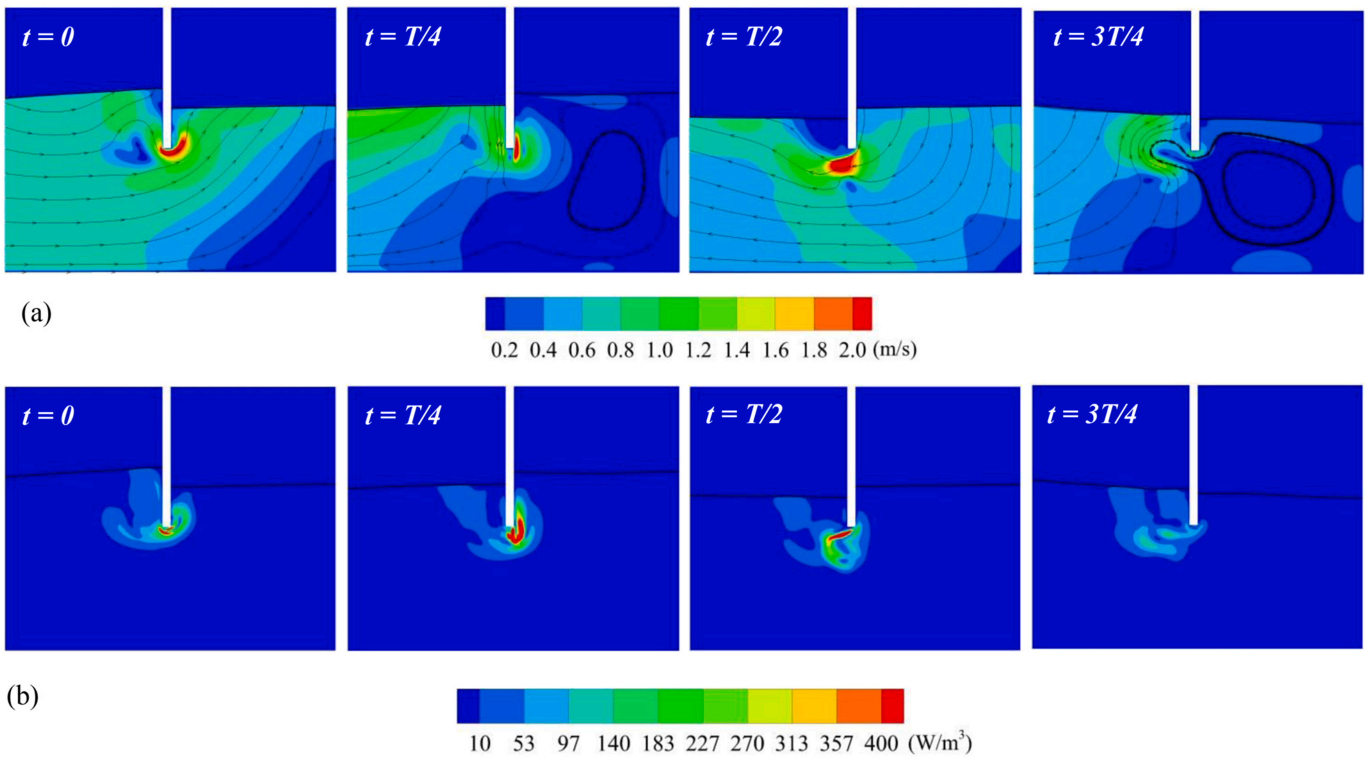

Fig. 8. Contours of (a) the velocity magnitude and streamlines and (b) energy rate losses due to the viscous and turbulence effects for the incident wave with $T = 8$ s and $H = 1.5$ m at four instants.

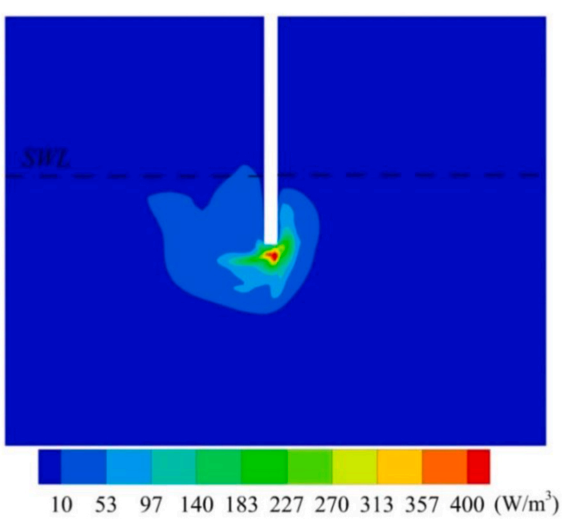

Fig. 9. Contour of the time average of the energy rate losses per volume due to the viscous and turbulence effects for the incident wave with $T = 8$ s and $H = 1.5$ m.

and C_R^2 for the range of wave periods from 6 to 12 s. It can be noticed that, although the E_R/E_{A0} is systematically higher than C_R^2, they have the same behavior, i.e., they maintain similar values from $T = 6$–7 s and, above this, increase with the wave period. Differences between E_R/E_{A0} and C_R^2 are from 0.04 to 0.08 along the wave period range. The highest perceptual difference occurs at $T = 6$ s (50%) and the lowest one is at $T = 12$ s (11%). It is important emphasizing that the three-gauge method is based on the Fourier analysis of signs of the free surface elevations and, consequently, it is expected that some complex wave behaviors are not captured, which can explain the differences observed. Moreover, there is the influence of uncertainties caused by the use of the active absorption technique on the wave maker, as already mentioned in previous cases of propagation and standing waves in a flume.

Another contribution of this analysis is to determine directly the quantity of each type of the mean energy rate of the process, by using the approximated formulation of the mean energy rate balance, Eq. (14), applied to a stable periodic regime. It is noticed that the mean energy rate E_B is practically null in all cases and, consequently, in the above composition this term is not computed. Fig. 10b shows percentages of the quantities $\%E_R$, $\%E_{L\mu}$ and $\%E_{Lp}$ in relation to the mean energy rate imposed by the wave maker (E_{A0}). Behaviors of curves obtained by the present methodology show that $\%E_{L\mu}$ is lower than the other quantities and varies from 6.8% ($T = 7$ s) to 3.6% ($T = 12$ s). The maximum value of $\%E_{Lp}$ is 80.8% at $T = 8$ s and the minimum one is 58.6% at $T = 12$ s. It

Table 4
Mean energy rates of the OWC device for incident wave period from 6 to 12 s.

T (s)	E_{A0} (kW/m)	E_A (kW/m)	E_R (kW/m)	E_B (kW/m)	$E_{L\mu}$ (kW/m)	E_{Lp} (kW/m)	ΔE_{tot} (kW/m)	Res (kW/m)	Res/E_{A0} (%)
6	15.86	13.88	1.96	0.00	0.85	12.43	0.04	0.54	3.4
7	18.42	16.42	2.00	0.00	1.26	14.64	0.02	0.50	2.7
8	20.34	17.86	2.48	0.00	1.07	16.43	0.00	0.36	1.8
9	21.89	18.04	3.85	0.00	0.98	16.79	0.02	0.26	1.2
10	23.20	17.04	6.17	0.00	0.92	16.00	0.03	0.08	0.4
11	24.48	16.96	7.52	0.00	1.27	15.37	0.04	0.28	1.1
12	25.36	15.97	9.39	0.00	0.91	14.85	0.00	0.23	0.9

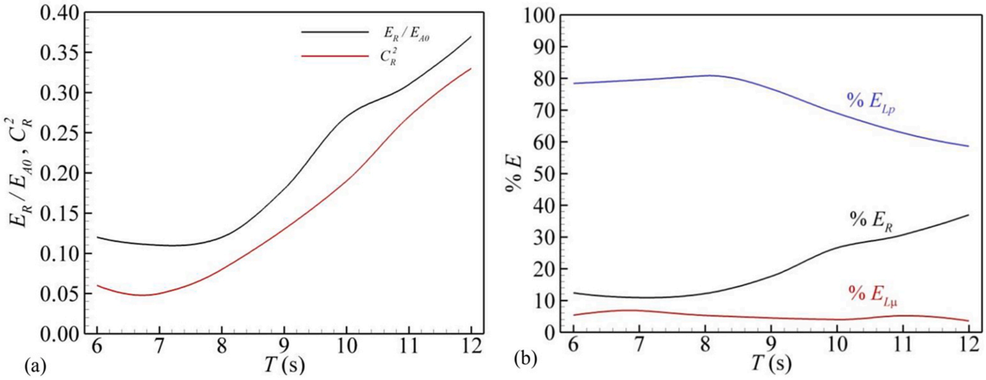

Fig. 10. (a) The mean reflected energy rate in relation to the mean energy rate imposed by the wave maker along the wave period by means of the proposal methodology (E_R/E_{A0}) and the three-gauge method (C_R^2). (b) Percentage of the mean energy rates along the wave period for the OWC device.

is important emphasizing that the reduction of $\%E_{Lp}$ with the wave period is synchronized with the increase of reflected wave by the OWC device, while the viscous and turbulence dissipation is maintained with little variation.

6. Wave over porous rubble-mound breakwaters

6.1. Study cases and mathematical models

In this study, two cases are analyzed: the wave over a porous low-crested rubble-mound breakwater, and the wave overtopping a rubble-mound breakwater. The former consists of a low-crested rubble–mound multilayered breakwater subject to incident regular waves, whose numerical analyses were previously carried out by Garcia et al. (2004) and Didier and Teixeira (2022). Fig. 11 shows the computational domain, in which the low-crested structure is positioned in the middle of the 8L long wave flume. The low-crested structure is composed of one armour layer (AL) and the core (CO), in which the hydraulic properties are shown in Didier and Teixeira (2022). Two incident regular waves, with $T = 1.6$ s, $H = 0.07$ m and $H = 0.10$ m are analyzed.

The second case consists of a rubble-mound breakwater subject to incident regular wave with $T = 6$ s and $H = 0.25$ m in a wave flume and wave overtopping, previously investigated by Losada et al. (2008) and Didier and Teixeira (2022), are carried out. Fig. 12 shows the computational domain, in which the rubble-mound breakwater with an impermeable caisson is founded on a horizontal bottom. The foundation is composed of a gravel core (CO) and intermediate (IL) and external (EL) layers, whose hydraulic properties are shown in Didier and Teixeira (2022). In both cases, the porous media, composed of armour layers and a core for rubble-mound breakwaters, are modeled by means of source terms S_i in the momentum equations, Eq. (16), according to Didier and Teixeira (2022).

6.2. Energy rate balance equation applied to porous rubble-mound breakwaters

The wave flume with a porous rubble-mound breakwater composes the system, whose sketch is shown in Fig. 13. The boundaries of the system are: the wave maker for wave generation (S_A), including active absorption; the end of the wave flume (S_B), in which the active absorption technique is applied to simulate a semi-infinite wave flume; the atmosphere; and the bottom (Fig. 13). The mean energy rate balance equation, Eq. (9), applied to the system, results in the following terms:

a) E_A is the mean energy rate measured at the wave maker boundary S_A, which is composed of the mean energy rate imposed to the wave maker boundary due to the incident wave (E_{A0}) deducted from the mean reflected wave energy rate (E_R);
b) E_B is the mean energy rate that passes through the end boundary of the wave flume S_B;
c) E_L is composed of:
   i The mean energy rate losses due to the fluid viscosity and turbulence effects ($E_{L\mu}$), and;
   ii The mean energy rate losses due to the porous rubble-mound breakwater that represents the damping of the transmitted water flow inside the medium (E_{Lp}), which is calculated by means of Eq. (13).

The mean reflected wave energy rate in relation to the mean incident wave energy rate (E_R/E_{A0}) is compared with the reflected wave coefficient squared (C_R^2), obtained by means of the three-gauge method, in which gauges are distant from the wave maker of 2L, 2.1L and 2.27L. Moreover, the mean transmitted wave energy rate in relation to the mean incident wave energy rate (E_B/E_{A0}) is compared with the transmitted coefficient squared (C_T^2), also obtained by the three-gauge method, in which gauges are located at the shoreward region, with the same distances from the breakwater as those of gauges used for measure the reflected wave have from the wave maker.

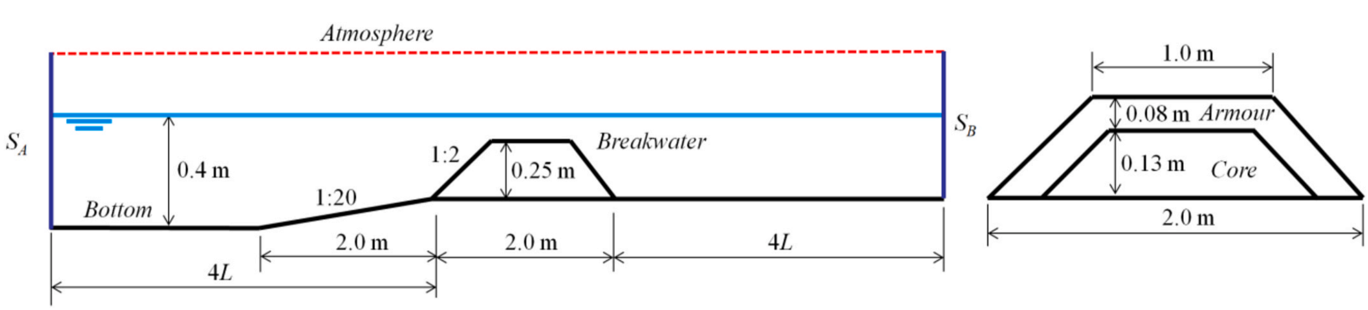

Fig. 11. Computational domain of the low-crested rubble–mound breakwater (Didier and Teixeira, 2022).

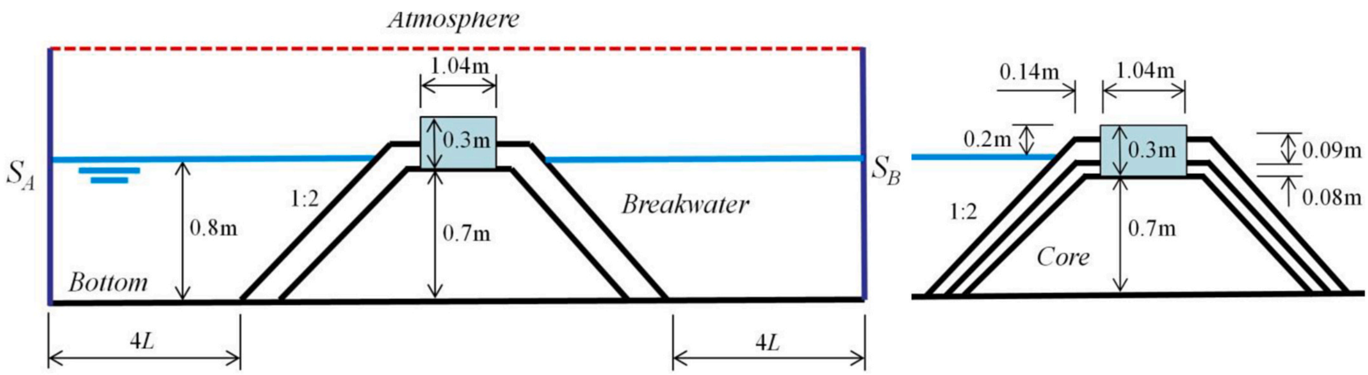

Fig. 12. Computational domain of the rubble-mound breakwater.

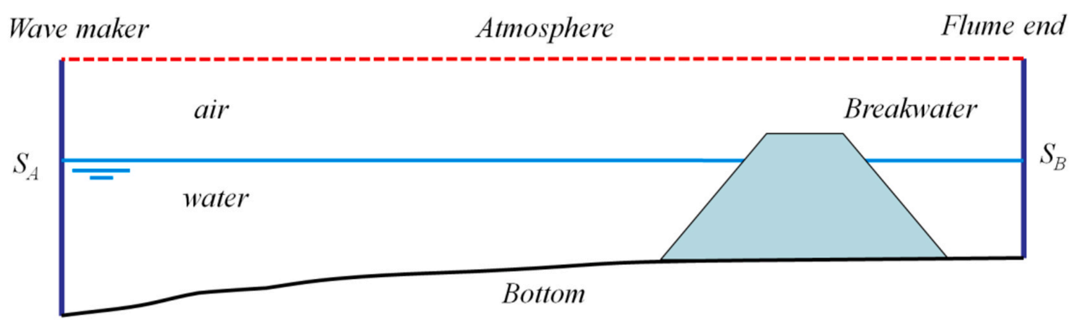

Fig. 13. Sketch of the computational domain for porous rubble-mound breakwater in a wave flume and variables of the energy rate balance.

6.3. Wave over a porous low-crested rubble-mound breakwater

Fig. 14 shows time series of the energy rate imposed by the wave maker ($\dot{E}_A$) and at the end of the flume ($\dot{E}_B$), the energy rate losses due to the viscosity and the turbulence effects at the flume ($\dot{E}_{L\mu f}$) and inside the breakwater ($\dot{E}_{L\mu b}$), the energy rate losses due to the resistances of the porous media ($\dot{E}_{Lp}$), and the total energy inside the numerical flume (E_{tot}) for the incident wave with $T = 1.6$ s and $H = 0.07$ m. The time series of the energy rate imposed by the wave maker ($\dot{E}_A$) stabilizes after initial little variations. The energy rate ($\dot{E}_B$) at the end boundary of the flume (S_B), located shoreward side of the breakwater, corresponds to the transmitted wave energy rate. It has a much lower magnitude than $\dot{E}_A$ due to the effect of the breakwater, which transforms the incident wave imposed by the wave maker. The energy rate due to viscous and turbulence losses ($\dot{E}_{L\mu f}$) in the flume corresponds to that out of the breakwater region and it is about 10^2 order of magnitude higher than $\dot{E}_{L\mu b}$, which corresponds to the one inside the breakwater. It is also observed some variability of $\dot{E}_{L\mu f}$ along the time caused by the wave breaking above the submerged rubble-mound breakwater. The time series of the energy rate due to the resistance of the porous media ($\dot{E}_{Lp}$) are shown in Fig. 14c. They are composed of the linear ($\dot{E}_{Lp1}$) and quadratic ($\dot{E}_{Lp2}$) terms, according to Eq. (8) for the armour layer (AL) and the core (CO). The quadratic term of the armour layer has the highest magnitude and both linear and quadratic terms of the core represent low resistances. The time variation of the total energy inside the numerical flume (E_{tot}), Fig. 14d, shows that stabilization is obtained after around 20 s.

Fig. 15 shows contours of the velocity magnitude, the energy rate per volume due to the viscous and turbulence losses and the dissipation in the porous zones of the submerged breakwater for $T = 1.6$ s and $H = 0.07$ m at four instants. It can be noticed that the energy rate per volume due to the viscous and turbulence losses is more intense above the submerged breakwater in the wave breaking region, whereas it is almost insignificant inside the porous zones. The dissipation due to the porous resistance inside the breakwater has more intensity in regions where the velocity magnitude is higher. It shows a higher energy rate per volume than the one due to viscous and turbulence effects. Besides, the armour layer has higher values of the energy rate per volume due to porous resistance, as expected in practical situations.

Fig. 16 shows the contour of the mean energy rate per volume due to the viscous and turbulence losses and the dissipation in the porous zones of the submerged breakwater for $T = 1.6$ s and $H = 0.07$ m. It can be noticed that the energy rate per volume due to the viscous and turbulence losses is more intense above the submerged breakwater (wave breaking region), whereas it is almost insignificant inside the porous zones. However, the dissipation due to the porous resistance inside the breakwater shows a higher mean energy rate per volume than the one due to viscous and turbulence effects. Besides, the seaward region of the armour layer is the one with the highest values of the mean energy rate per volume due to porous resistance, since this zone of the submerged breakwater is exposed to the incident wave and high velocity magnitudes.

Fig. 17 shows contours of the velocity magnitude, the energy rate per volume due to the viscous and turbulence losses and the dissipation in the porous zones of the submerged breakwater for $T = 1.6$ s and $H = 0.10$ m at four instants. It is observed similar spatial distributions of both variables in relation to those noticed for an incident wave with $H = 0.07$ m because wave breaking occurs more or less in the same zone above and slightly after the submerged breakwater. However, the intensity of the energy rate above the breakwater due to viscous and turbulence losses is much higher, which is probably due to a higher energy wave breaking induced by the higher wave height. The spatial distribution of the intensity of the energy rate due to porous resistance follows regions where the velocity magnitude is higher, and it is more intense in the armour layer and seaward region of the submerged breakwater.

Fig. 18 shows the contour of the mean energy rate per volume due to the viscous and turbulence losses and the dissipation in the porous zones of the submerged breakwater for $T = 1.6$ s and $H = 0.10$ m. It is observed similar spatial distributions of both variables in relation to those noticed

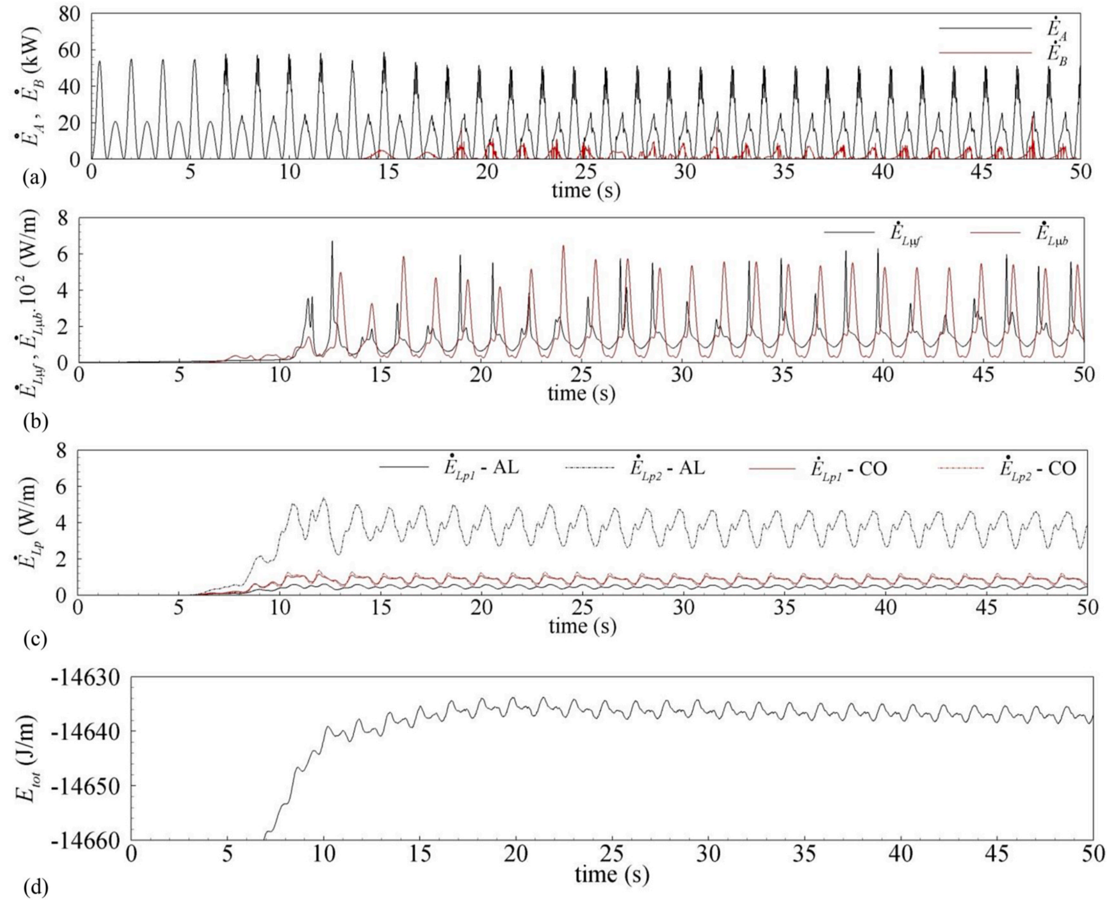

Fig. 14. Low-crested rubble-mound breakwater for the incident wave with $T = 1.6$ s and $H = 0.07$ m: (a) the energy rate imposed by the wave maker and at the end of the flume, (b) the energy rate due to the viscosity and the turbulence losses, (c) the energy rate due to the resistances of the porous media, and (d) the total energy inside the numerical flume.

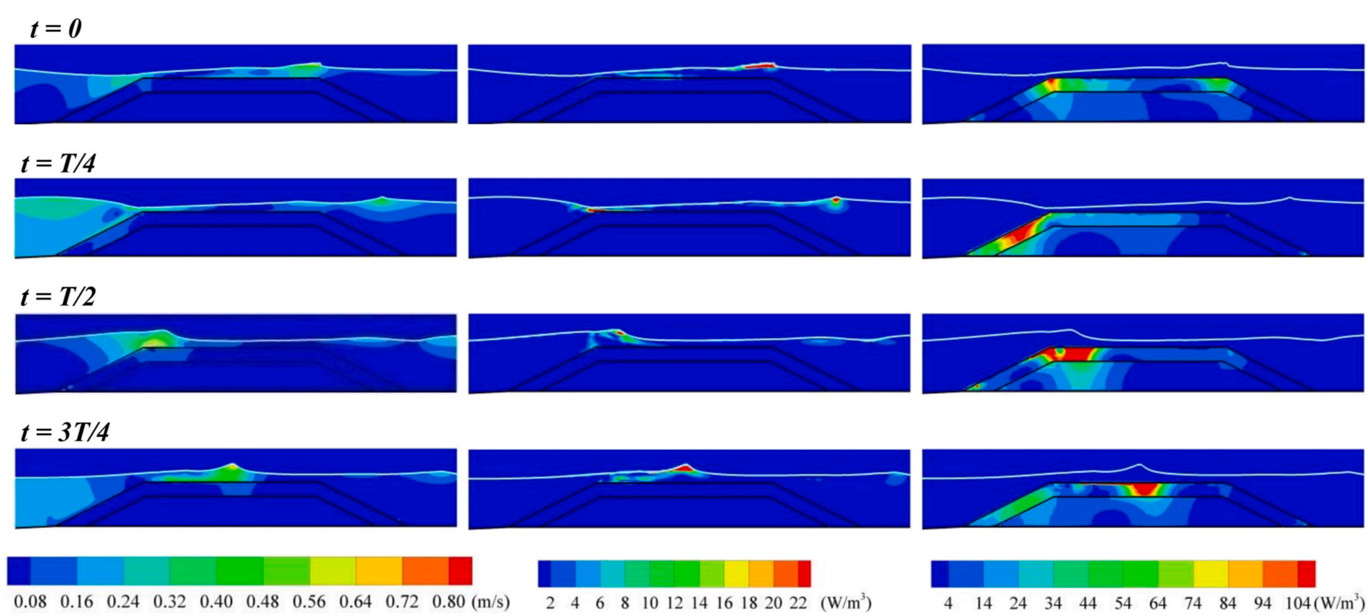

Fig. 15. Contours of the velocity magnitude (first column), the energy rate per volume due to the viscous and turbulence losses (second column) and the dissipation in the porous zones per volume (third column) of the submerged breakwater for $T = 1.6$ s and $H = 0.07$ m.

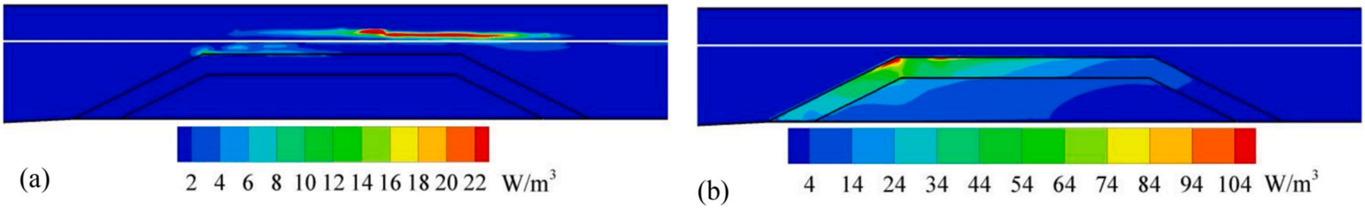

Fig. 16. Contour of the mean energy rate per volume for $T = 1.6$ s and $H = 0.07$ m due to the (a) viscous and turbulence losses and (b) the dissipation in the porous zones per volume of the submerged breakwater.

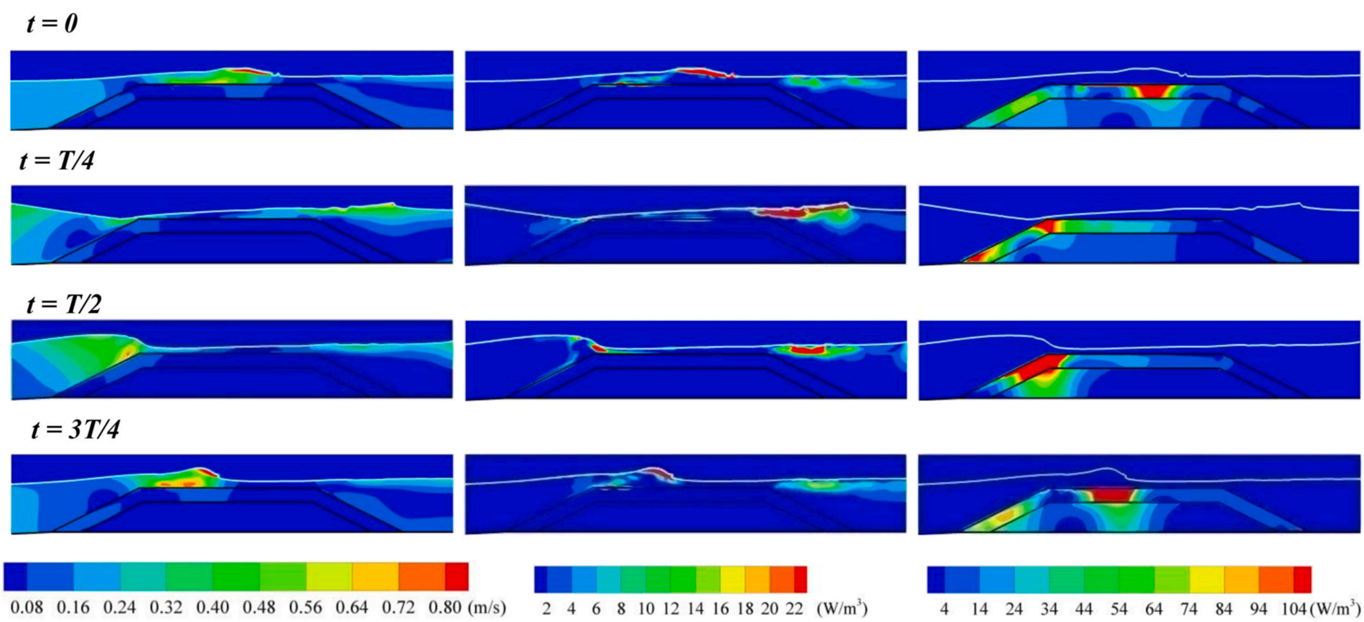

Fig. 17. Contours of the velocity magnitude (first column), the energy rate per volume due to the viscous and turbulence losses (second column) and the dissipation in the porous zones per volume (third column) of the submerged breakwater for $T = 1.6$ s and $H = 0.10$ m.

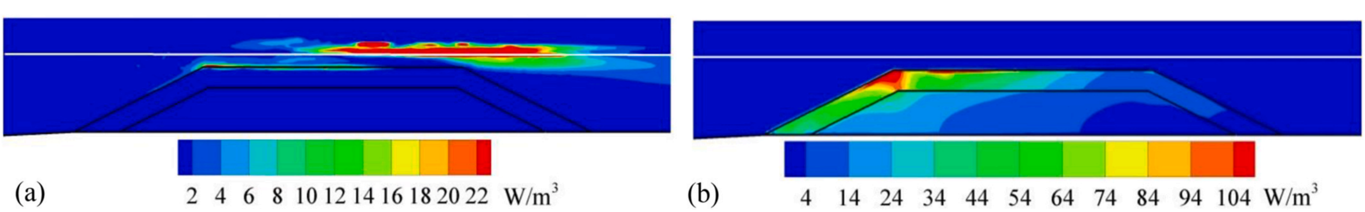

Fig. 18. Contour of the mean energy rate per volume for $T = 1.6$ s and $H = 0.10$ m due to the (a) viscous and turbulence losses and (b) the dissipation in the porous zones of the submerged breakwater.

for an incident wave with $H = 0.07$ m. However, the intensity of the energy rate above the breakwater due to viscous and turbulence losses is much higher and occurs slightly after the submerged breakwater, probably because of the higher energy wave breaking. Moreover, the intensity of the energy rate due to viscous and turbulence losses in the core is very small compared to that caused by the porous resistance.

Table 5 shows mean energy rates for the low-crested rubble–mound breakwater case. Residues of both cases are very low, although it is more significant for $H = 0.07$ m. It can be noticed that the mean energy rate inside the flume (ΔE_{tot}) in both cases is very low in relation to the mean energy rate of the incident wave imposed by the wave maker (E_{A0}). Moreover, the mean energy rate due to viscous and turbulence losses ($E_{L\mu}$) in the case $H = 0.10$ m is higher than the one in the case $H = 0.07$ m, which is probably due to a stronger energetic wave breaking above the submerged breakwater, as observed previously. The mean energy rate due to the porous zones inside the armour layer, $E_{Lp(AL)}$, is around 70% of the mean energy rate (E_{Lp}) in both cases, which means that a large part of dissipation that occurs in the submerged breakwater is due

Table 5
Mean energy rates for the low-crested rubble–mound breakwater.

T (s)	H (m)	E_{A0} (W/m)	E_A (W/m)	E_R (W/m)	E_B (W/m)	$E_{L\mu f}$ (W/m)	$E_{L\mu b}$ (W/m)	$E_{Lp(AL)}$ (W/m)	$E_{Lp(CO)}$ (W/m)	ΔE_{tot} (W/m)	Res (W/m)	Res/E_{A0} (%)
1.6	0.07	8.63	8.26	0.37	0.67	1.67	0.02	4.03	1.67	0.02	0.18	2.1
1.6	0.10	17.57	15.99	1.58	1.58	5.43	0.09	6.17	2.49	0.38	−0.15	−0.9

to the external layer.

The relation between the mean reflected energy rate and the mean energy rate imposed by the wave maker (E_R/E_{A0}) is 0.04 for $H = 0.07$ m, whereas it is obtained a similar value, $C_R^2 = 0.03$, by using the three-gauge method. In the case of $H = 0.10$ m, E_R/E_{A0} is 0.09 and $C_R^2 = 0.03$, which indicates some differences, although both values are low. The relation between the mean transmitted energy rate and the mean energy rate imposed by the wave maker (E_B/E_{A0}) is 0.08 and 0.09 for $H = 0.07$ and 0.10 m, respectively, whereas $C_T^2 = 0.08$ for both cases by using the three-gauge method, which shows a very good agreement.

The mean incident wave energy rate (E_{A0}) is composed of each type of mean energy rate of the system in a stable periodic regime, as formulated in Eq. (14). In these study cases, the mean energy rates reflected by the submerged breakwater (E_R) are 4.4 and 9.1% of the mean incident wave energy rate, for $H = 0.07$ and 0.10 m, respectively. The mean energy rates transmitted after the breakwater (E_B) are 7.9 and 9.1%, respectively. The dissipation of the mean energy rates has contributions of the breakwater ($E_{L\mu b} + E_{Lp}$), which corresponds to approximately 67.9 and 50.5% of the mean incident wave energy rate, for $H = 0.07$ and 0.10 m, respectively; and the viscous and turbulence dissipations of the fluid out of the breakwater, mainly due to the wave breaking ($E_{L\mu f}$), that are 19.8 and 31.3%, respectively. Therefore, this analysis allows understanding in detail the influence of each phenomenon on the mean transmitted energy rate due to the presence of the submerged breakwater on the flume.

6.4. Wave overtopping a rubble-mound breakwater

Fig. 19 shows the time series of the energy rate imposed by the wave maker ($\dot{E}_A$) and at the end of the flume ($\dot{E}_B$), the energy rate losses due to the viscosity and the turbulence effects ($\dot{E}_{L\mu}$), the energy rate losses due to the resistances of the porous media ($\dot{E}_{Lp}$), and the total energy inside the numerical wave flume (E_{tot}). The time series of the energy rate imposed by the wave maker ($\dot{E}_A$) stabilizes after initial little variations. The energy rate at the end boundary of the flume ($\dot{E}_B$) has a much lower magnitude than $\dot{E}_A$ due to the presence of the breakwater, which filters the incident wave, causing a decrease in the transmitted energy rate. The energy rate due to viscous and turbulence losses in the flume ($\dot{E}_{L\mu f}$) is about 10^1 order of magnitude higher than $\dot{E}_{L\mu b}$, which corresponds to the one inside the breakwater. $\dot{E}_{Lp}$ inside the breakwater core is much higher than those of external and intermediate layers as observed in Fig. 19c. The time variation of the total energy inside the numerical flume (E_{tot}), Fig. 19d, shows that there is stabilization after around 140 s.

Fig. 20 shows contours of the velocity magnitude, the energy rate per volume due to the viscous and turbulence losses and the dissipation in the porous zones of the breakwater at four instants, in which the crest of the incident wave is propagating along the breakwater until the overtopping at the impermeable caisson. It can be noticed that the energy rate per volume due to the viscous and turbulence losses is more intense around the wave breaking region, above and after the impermeable caisson, and inside the external armour layer, especially at the seaward side. However, it is almost insignificant inside the internal porous zones,

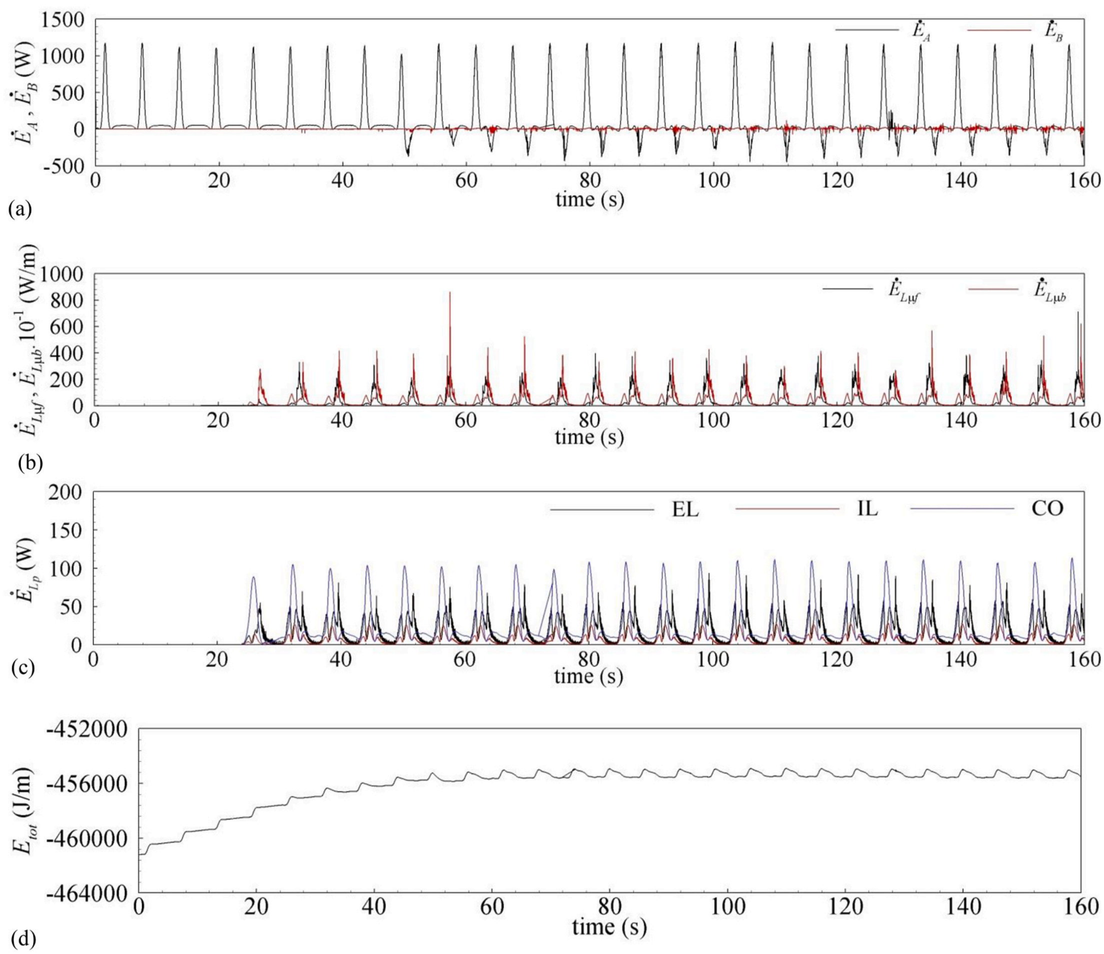

Fig. 19. Rubble-mound breakwater: Time series of (a) energy rate imposed by the wave maker and at the end of the flume, (b) energy rate due to the viscosity and the turbulence losses, (c) energy rate due to the resistances of the porous media, and (d) total energy inside the numerical flume.

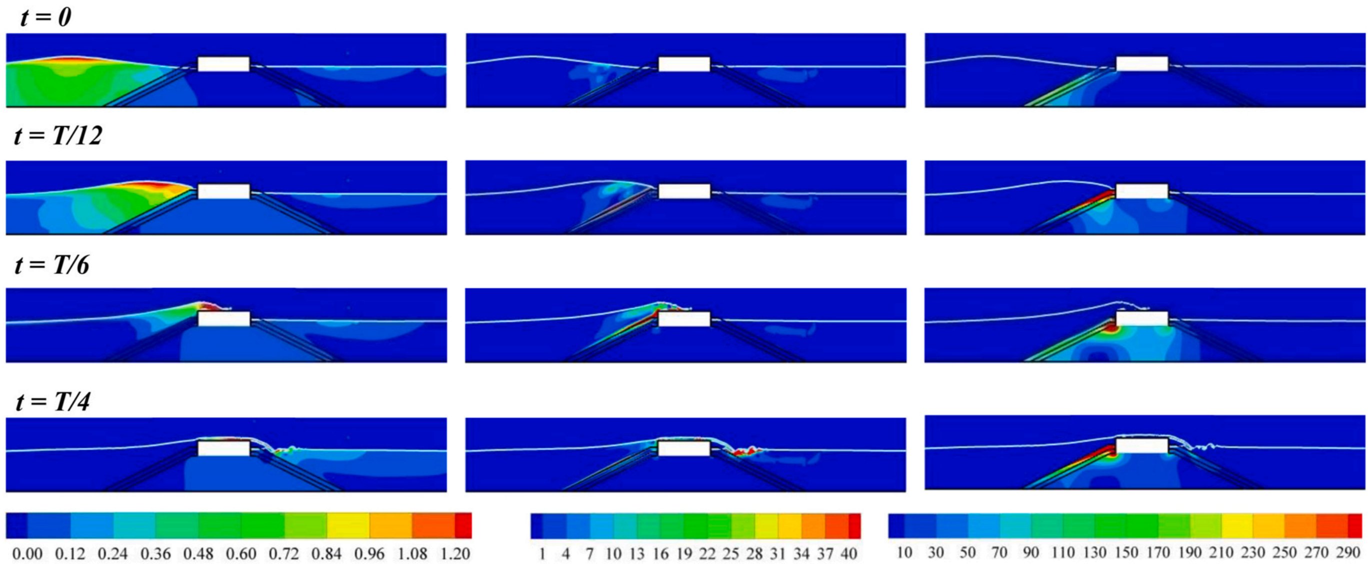

Fig. 20. Contours of the velocity magnitude in m/s (first column), the energy rate per volume due to the viscous and turbulence losses (second column) and the dissipation in the porous zones per volume in W/m^3 (third column) of the rubble-mound breakwater.

i.e., in the intermediate layer and the core. The dissipation due to the porous resistance has a higher energy rate per volume than the one due to viscous and turbulence effects. The energy rate per volume due to porous resistance inside the breakwater has more intensity in the external layer. However, a significant dissipation is also observed in the gravel core.

Fig. 21 shows the contour of the mean energy rate per volume due to the viscous and turbulence losses and the dissipation in the porous zones of the breakwater. The energy rate per volume due to the viscous and turbulence losses is more intense around the free surface shoreward, due to the wave overtopping and the water jet induced above the impermeable caisson, which causes a complex mixture flow interaction in the free surface shoreward. However, it is almost insignificant inside the porous zones. The external and intermediate layers have the highest values of the mean energy rate per volume due to porous resistance, since they are directly subjected to the wave impact. There are significant values at the gravel core, mainly at the seaward region.

Table 6 shows the mean energy rates. The time variation of the total energy inside the flume (ΔE_{tot}) is about 0.3% of the incident wave energy rate imposed by the wave maker (E_{A0}), which represents a practical stabilization. The residue is very low in relation to the incident wave energy rate (around 1.3% of E_{A0}), indicating that the proposal methodology is adequate. The mean energy rate due to viscous and turbulent losses ($E_{L\mu}$) has the same order of magnitude as the total mean energy rate due to porous media (E_{Lp}). The mean energy rate due to porous media in the core is higher than the ones in the layers, because of its higher volume. However, even with much less volume, the external layer presents a significant value of this type of the mean energy rate, since this region is subject to the direct impact of the wave and the wave overtopping phenomenon on the seaward and shoreward side of the breakwater, respectively.

The relation between the mean reflected energy rate and the mean energy rate imposed by the wave maker (E_R/E_{A0}) is 0.30, whereas $C_R^2 = 0.42$, by using the three-gauge method. The mean energy rate transmission (E_B) is low in this case, which corresponds to E_B/E_{A0} of about 0.06; C_T^2 obtained by the three-gauge method is 0.04.

In this case, the mean energy rate reflected by the breakwater (E_R) is 29.2% of the mean incident wave energy rate and the mean transmitted energy rate (E_B) is 5.6%. The dissipation of the mean energy rate of the breakwater ($E_{L\mu b} + E_{Lp}$) is 38.0% of the mean incident wave energy rate. The viscous and turbulence dissipation of the fluid out of the breakwater ($E_{L\mu f}$) is 27.2% and, therefore, it corresponds to a significant contribution to the damping effect of the wave due to the presence of the breakwater.

7. Conclusion

In this study, a novel methodology is developed to evaluate the energy rate balance of coastal engineering systems by means of RANS-based numerical models. Energy rates due to viscosity, turbulence and porous medium losses are evaluated directly in cases of incident regular waves in numerical flumes. The mean energy rate balance equation of the system is verified with very low residue, which confirms the correct numerical calculation of the various quantities.

The methodology was applied in different systems, which represent typical coastal engineering problems: progressive and standing waves in a numerical flume; regular waves over an onshore OWC device; regular waves over a low-crested rubble–mound breakwater; and wave overtopping of a rubble-mound breakwater.

The proposal methodology allows quantifying each type of energy of the system, which is very important to the system design. A good contribution is the direct determination of the mean reflected and

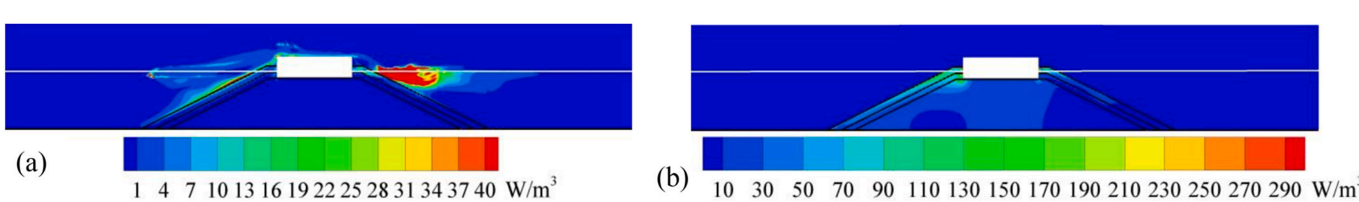

Fig. 21. Contour of the mean energy rate per volume due to the (a) viscous and turbulence losses and (b) the dissipation in the porous zones of the rubble-mound breakwater.

Table 6
Mean energy rates for the rubble-mound breakwater.

T (s)	E_{A0} (W/m)	E_A (W/m)	E_R (W/m)	E_B (W/m)	$E_{L\mu f}$ (W/m)	$E_{L\mu b}$ (W/m)	E_{LpEL} (W/m)	E_{LpIL} (W/m)	E_{LpCO} (W/m)	ΔE_{tot} (W/m)	Res (W/m)	Res/E_{A0} (%)
6	151.35	106.66	44.69	8.61	41.52	4.55	20.73	7.49	25.28	0.38	−1.90	−1.3

transmitted energy rates that occur in a numerical flume due to the presence of a coastal structure. This technique was compared to the standard methodology named the three-gauge method, which is based on the calculation of the reflected coefficient by means of three gauges located in different positions on the flume. It was observed that, in certain cases, values are in good agreement, but some differences were found in other cases. Probably because the three-gauge method is based on the Fourier analysis of signs of the free surface elevations, in which some complex wave behaviors are not captured. Therefore, the proposed method is a very good option to obtain numerically de reflected and the transmitted wave energy rates inside the flume.

Another contribution is the evaluation of the mean energy rate due to viscous and turbulence losses in the system. The methodology allows determining the spatial distribution of this quantity and, consequently, observing which region has the highest energy dissipation. In the case of the onshore OWC device, the standard techniques calculate the mean energy dissipation by considering that it is the difference between the theoretical energy imposed by the wave maker and reflected and energy losses due to the air turbine installed in the chamber. Therefore, in the case of standard techniques, the mean energy rate due to viscous and turbulence losses is not determined directly, differently of the proposal methodology. Besides, in the case of the onshore OWC device, it was noticed accurately the region where the turbulence dissipation has the highest intensity, allowing designers study different geometrical configurations to have better device efficiency. It may be emphasized that the present methodology can be applied to different types of wave energy converters.

The direct evaluation of the mean energy rate due to the flow resistance of porous media is another important contribution of the present methodology. It allows, for example, determining the energy rate dissipation of each layer of a rubble–mound breakwater, providing important information to coastal design engineers.

The low order of the numerical uncertainties, measured based on the residue of the rate energy balance applied to the study cases, show that the proposed methodology has adequate accuracy. It can be applied to any type of coastal engineering system by using numerical models based on the Navier-Stokes equations. The main contribution of the technique is to allow a better understanding of the physical processes of wave-structure interactions and, consequently, it may be a useful tool to be applied to design coastal and harbor structures and wave energy converter devices. Complement studies may be carried out for random incident waves and the methodology can be applied to 3D wave tanks.

CRediT authorship contribution statement

Teixeira P.R.F: Writing – original draft, Validation, Supervision, Project administration, Methodology, Investigation, Funding acquisition, Formal analysis, Conceptualization. **Didier E:** Writing – review & editing, Supervision, Methodology, Investigation, Formal analysis.

Declaration of competing interest

The authors declare that they have no known competing financial interests or personal relationships that could have appeared to influence the work reported in this paper.

Acknowledgements

The authors acknowledge the cooperation between the Universidade Federal do Rio Grande – FURG, Brazil, and the Laboratório Nacional de Engenharia Civil – LNEC, Portugal. The first author acknowledges the support of CNPq (project 307546/2921-7) and FAPERGS (project 21/2551-0002014-8).

References

Ansys, 2016. FLUENT—User's Guide. ANSYS Inc., Canonsburg, PA, USA.
Bird, R.B., Stewart, W.E., Lightfoot, E.N., 2002. Transport Phenomena, second ed.
Brown, S.A., Greaves, D.M., Magar, V., Conley, D.C., 2016. Evaluation of turbulence closure models under spilling and plunging breakers in the surf zone. Coast. Eng. 114, 177–193.
Dean, R.G., Dalrymple, R.A., 2000. Water Wave Mechanics for Engineers and Scientists. World scientific publishing Co. Pte. Ltd., London.
del Jesus, M., Lara, J.L., Losada, I.J., 2012. Three-dimensional interaction of waves and porous structures. Part I: numerical model formulation. Coast. Eng. 64, 57–72.
Devolver, B., Trouch, P., Rauwoens, P., 2018. Performance of a buoyancy-modified k-ω and k-ω SST turbulence model for simulating wave breaking under regular waves using OpenFOAM. Coast. Eng. 138, 49–65.
Didier, E., Teixeira, P.R.F., Neves, M.G., 2017. A 3D numerical wave tank for coastal engineering studies. Defect Diffusion Forum 372, 1–10.
Didier, E., Teixeira, P.R.F., 2022. Validation and comparisons of methodologies implemented in a RANS-VoF numerical model for applications to coastal structures. J. Mar. Sci. Eng. 10, 1298.
Didier, E., Teixeira, P.R.F., 2023. A RANS-based numerical model to simulate overtopping-type wave energy converters integrated into breakwaters. Int. J. Offshore Polar Eng. 33, 420–427.
Didier, E., Teixeira, P.R.F., 2024. Numerical analysis of 3D hydrodynamics and performance of an array of oscillating water column wave energy converter integrated into a vertical breakwater. Renew. Energy 225, 120297.
Elhanafi, A., Fleming, A., Macfarlane, G., Leong, Z., 2016. Numerical energy balance analysis for an onshore oscillating water column wave energy converter. Energy 116, 539–557.
Garcia, N., Lara, J., Losada, I., 2004. 2-D numerical analysis of near-field flow at low-crested permeable breakwaters. Coast. Eng. 51, 991–1020.
Güths, A.K., Teixeira, P.R.F., Didier, E., 2022. A novel geometry of an onshore Oscillating Water Column wave energy converter. Renew. Energy 201, 938–949.
Higuera, P., Lara, J.L., Losada, I.J., 2014. Three-dimensional interaction of waves and porous coastal structures using OpenFOAM. Part I: formulation and validation. Coast. Eng. 83, 243–258.
Hirt, C.W., Nichols, B.D., 1981. Volume of fluid VOF method for the dynamics of free boundaries. Journal of Computers and Physics 39 (1), 201–225.
Hsu, T.-J., Sakakiyama, T., Liu, P.L.-F., 2002. A numerical model for wave motions and turbulence flows in front of a composite breakwater. Cost Eng. 46, 25–50.
Larsen, B.E., Fuhrman, D.R., 2018. On the over-production on turbulence beneath surface waves in Reynolds-averaged Navier-Stokes models. J. Fluid Mech. 853, 419–460.
Lin, P., Liu, P.L.-F., 1998. A numerical study of breaking waves in the surf zone. J. Fluid Mech. 359, 239–264.
Lisboa, R.C., Teixeira, P.R.F., Didier, E., 2017. Regular and irregular wave propagation analysis in a flume with numerical beach using a Navier-Stokes based model. Defect Diffusion Forum 372, 81–90.
Lisboa, R.C., Teixeira, P.R.F., Torres, F.R., Didier, E., 2018. Numerical evaluation of the power output of an oscillating water column wave energy converter installed in the southern Brazilian coast. Energy 162, 1115–1124.
Losada, I.J., Lara, J.L., Guauche, R., Gonzales-Ondina, J.M., 2008. Numerical analysis of wave overtopping of rubble mound breakwaters. Coast. Eng. 55, 47–62.
Mansard, E.P.D., Funke, E.R., 1980. The Measurement of incident and reflected spectra using a least squares method. Coast Eng. 4, 154–174.
Mendonça, A., Dias, J., Didier, E., Fortes, C.J.E.M., Neves, M.G., Reis, M.T., Conde, J.M.P., Poseiro, P., Teixeira, P.R.F., 2018. An integrated tool for modelling OWC-WECs in vertical breakwaters: preliminary developments. Journal of Hydro-environment Research 19, 198–213.
Nield, D.A., 2002. Modelling fluid flow in saturated porous media and at interfaces. In: Ingham, D.B., Pop, I. (Eds.), Transport Phenomena in Porous Media II. Pergamon, London, pp. 1–19.
Opoku, F., Uddin, M.N., Atkinson, M., 2023. A review of computational methods for studing oscillating water columns – the Navier-Stokes based equation approach. Renew. Sustain. Energy Rev. 174, 113124.
Penalba, M., Giorgi, G., Ringwood, J.V., 2017. Mathematical modelling of wave energy converters: a review of nonlinear approaches. Renew. Sustain. Energy Rev. 78, 1188–1207.
Péric, M., Ferziger, J.H., 1997. Computational Methods for Fluid Dynamics, second ed. Springer, Berlin.

Shih, T.-H., Zhu, J., 1996. Calculation of wall-bounded complex flows and free shear flows. Int. J. Numer. Methods Fluid. 23, 1133–1144.
Teixeira, P.R.F., Didier, E., Neves, M.G., 2017. A 3D RANS-VOF wave tank for oscillating water column device studies. VII International Conference on Computational Methods in Marine Engineering – MARINE, Nantes 710–721.
Teixeira, P.R.F., Gonçalves, R.A.A.C., Didier, E., 2020. A RANS-VoF numerical model to analyze the output power of an OWC-WEC equipped with wells and Impulse turbines in A hypothetical sea-state. China Ocean Eng. 34 (6), 760–771.
Teixeira, P.R.F., Didier, E., 2021. Numerical analysis of the response of an onshore oscillating water column wave energy converter to random waves. Energy 220, 119719.
Teixeira, P.R.F., Didier, E., 2023. Numerical analysis of performance of an oscillating water column wave energy converter inserted into a composite breakwater with rubble mound foundation. Ocean Eng. 278, 114421.
Tseng, R.S., Wu, R.H., Huang, C.C., 2000. Model study of a shoreline wave-power system. Ocean Eng. 27, 801–821.
Vafai, K., 2005. Handbook of Porous Media, 2a Ed.
van Gent, M.R.A., 1995. Porous flow through rubble-mound material. J. Waterw. Port, Coast. Ocean Eng. 121 (3), 176–181.
Vanneste, D., Troch, P., 2015. 2D numerical simulation of large-scale physical model tests of wave interaction with a rubble-mound breakwater. Coast. Eng. 103, 22–41.
Versteeg, H.K., Malalasekera, W., 2007. An Introduction to Computational Fluid Dynamics: the Finite Volume Method. Pearson Education Limited.
Whitaker, S., 1999. The method of volume averaging. In: Theory and Applications of Transport in Porous Media, vol. 13. Kluwer Academic.
Wiener, G.F., Teixeira, P.R.F., Didier, E., 2022. Numerical evaluation of optimal sizes of wells turbine and chamber of a cluster of oscillating water columns integrated into a breakwater on the southern Brazilian coast. J. Waterw. Port, Coast. Ocean Eng. 148 (4), 04022009.
Windt, C., Davidson, J., Ringwood, J.V., 2018. High-fidelity modelling of ocean wave energy systems: a review of computational fluid dynamics-based nuerical wave tanks. Renewable ans Sustainable Energy Reviews 93, 601–630.